EIC-ESR Polarization

Matt Signorelli

This text was adapted from Chapters 3, 4, 6, and 7 of my PhD thesis *Electron spin polarization preservation in the Electron-Ion Collider*.

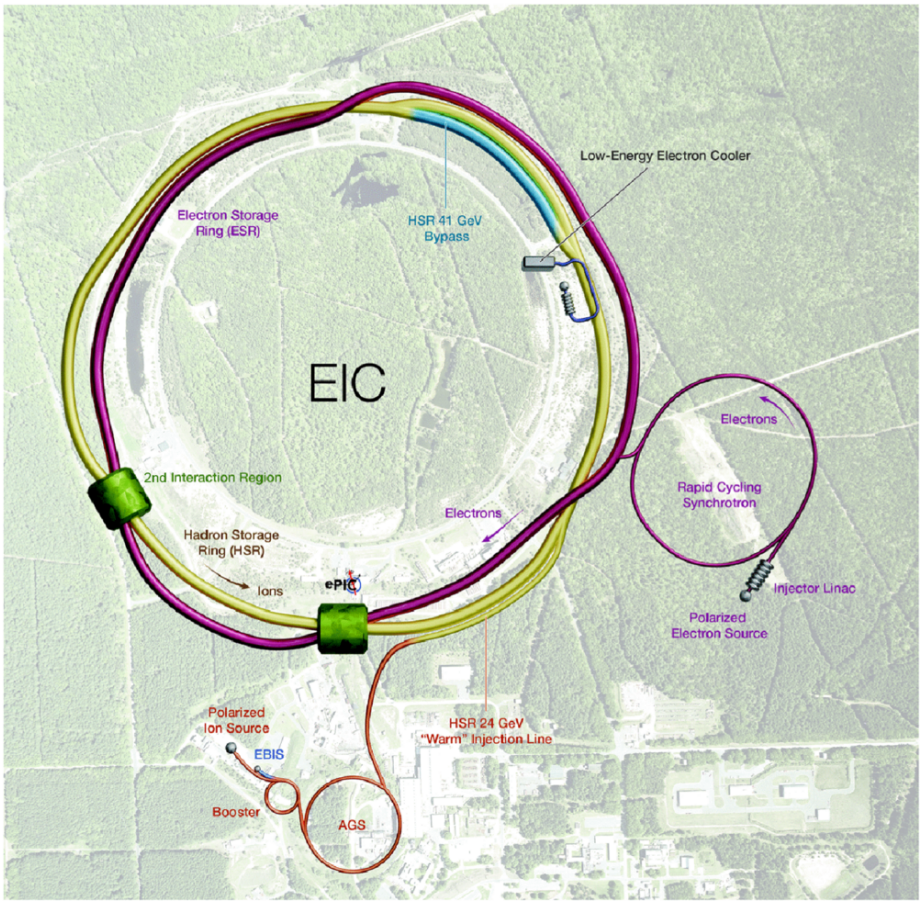

Figure 1: Conceptual schematic of the Electron-Ion Collider.

1 Theory

1.1 Electron Bunch Polarization Time Evolution

The ultimate goal in designing spin polarized rings is to minimize the mechanisms and rates at which spin actions in a beam may be reduced. For electrons in storage rings, bunch polarization evolution is largely dominated by the stochastic emission of synchrotron radiation, which causes three effects: (1) the *Sokolov-Ternov (ST) effect* which is an asymmetry in the spin flip rate during photon emission leading to a buildup of polarization antiparallel to the bending field for electrons at a rate τ_{st}^{-1}, (2) *radiative depolarization* where the instantaneous jump in phase space coordinates after photon emission changes a particle's spin action and rapidly reduces the polarization of a bunch at a rate

τ_{dep}^{-1}, and (3) *kinetic polarization* where the asymmetry of the photon emission causes particles' spins to occasionally be more aligned with the ISF on average after photon emission [25, 2, 3, 9]. The effect of kinetic polarization is only significant when $\hat{\boldsymbol{n}}_0$ is not vertical in significant portions of the ring. All three of these effects balance each other out over time leading to an asymptotic polarization for ultra-relativistic electrons given by the Derbenev-Kondratenko (DK) formula [9],

$$P_{dk} = \frac{8}{5\sqrt{3}} \frac{\oint ds \left\langle |\dot{\hat{\boldsymbol{v}}}|^3 \, \hat{\boldsymbol{b}} \cdot (\hat{\boldsymbol{n}} - \boldsymbol{d}) \right\rangle}{\oint ds \left\langle |\dot{\hat{\boldsymbol{v}}}|^3 \left(1 - \frac{2}{9}(\hat{\boldsymbol{n}} \cdot \hat{\boldsymbol{v}})^2 + \frac{11}{18} |\boldsymbol{d}|^2\right) \right\rangle} \,, \tag{1}$$

where $\hat{\boldsymbol{v}}$ is a unit vector in the direction of the particle's velocity, $\dot{\hat{\boldsymbol{v}}}$ is the curvature of the particle trajectory, $\hat{\boldsymbol{b}} = \hat{\boldsymbol{v}} \times \dot{\hat{\boldsymbol{v}}}/|\dot{\hat{\boldsymbol{v}}}|$, $\langle ... \rangle$ denotes an average over the particle ensemble, s is the arc position along the closed orbit, and $\boldsymbol{d} = \gamma_0 \frac{\partial \hat{\boldsymbol{n}}}{\partial \gamma}$ is the so-called *spin-orbit coupling function*. The spin-orbit coupling function captures the dependence of the ISF with energy, and thus defines the degree of radiative depolarization present in a ring. In Eq. (1), the $\hat{\boldsymbol{b}} \cdot \boldsymbol{d}$ term corresponds to the kinetic polarizing mechanism, $\frac{11}{18}|\boldsymbol{d}|^2$ term to the radiative depolarization, and the remaining terms to the Sokolov-Ternov effect. The time evolution of a bunch's polarization is

$$P(t) = P_{dk}(1 - e^{-t/\tau_{dk}}) + P_0 e^{-t/\tau_{dk}} \,, \tag{2}$$

where $\tau_{dk}^{-1} = \tau_{st}^{-1} + \tau_{dep}^{-1}$, and P_0 is the initial bunch polarization. The Sokolov-Ternov rate and radiative depolarization rate are respectively

$$\tau_{st}^{-1} = \frac{5\sqrt{3}}{8} \frac{r_e \gamma_0^5 \hbar}{m_e} \frac{1}{C} \oint ds \left\langle |\dot{\hat{\boldsymbol{v}}}|^3 \left(1 - \frac{2}{9}(\hat{\boldsymbol{n}} \cdot \hat{\boldsymbol{v}})^2\right) \right\rangle \,, \tag{3}$$

$$\tau_{dep}^{-1} = \frac{5\sqrt{3}}{8} \frac{r_e \gamma_0^5 \hbar}{m_e} \frac{1}{C} \oint ds \left\langle |\dot{\hat{\boldsymbol{v}}}|^3 \frac{11}{18} |\boldsymbol{d}|^2 \right\rangle \,, \tag{4}$$

where r_e is the classical electron radius, m_e is the electron mass, and C is the circumference of the ring.

For electron rings, the primary task is to reduce $\boldsymbol{d}$ around the ring as much as possible, thus minimizing the radiative depolarization rate and maximizing the asymptotic polarization. In a perfectly midplane symmetric ring without spin rotators, $\boldsymbol{d}$ is already zero everywhere; in such a case the vertical beam size is approximately zero due to radiation damping, and the beam (which lies entirely in the midplane) only sees vertical magnetic fields. The ISF is therefore fully vertical in all occupied areas of phase space. However, once $\hat{\boldsymbol{n}}_0$ is rotated out of the vertical (e.g. by spin rotators or random errors), $\boldsymbol{d}$ will be excited and cause rapid radiative depolarization if left uncorrected.

1.2 First-Order Spin-Orbit Motion

It can be insightful to consider the theory in a simplified model. In this section, we invoke the paraxial approximation and consider the dynamics to first-order in deviations from the closed orbit. Still using a coordinate system that has its origin on the closed orbit ($\boldsymbol{\zeta}_{\text{c.o.}} = \mathbf{0}$), we linearize in $\boldsymbol{\zeta}$ for small deviations around the closed orbit. We also linearize in deviations of the trace space coordinates x', y', where $'$ denotes differentiation with respect to the arc position along the closed orbit s. We define the right-handed orthonormal coordinate system $(\hat{\boldsymbol{x}}(s), \hat{\boldsymbol{y}}(s), \hat{\boldsymbol{s}}(s))$ along the closed orbit (note that $\hat{\boldsymbol{y}}$ may not always point vertically with respect to the geometric layout of the accelerator, for example). The local horizontal and vertical curvatures of the coordinate system are specified by $\boldsymbol{g} = g_x\hat{\boldsymbol{x}} + g_y\hat{\boldsymbol{y}}$. In the absence of electric fields, by definition $g_x = \frac{q}{p_0}B_y|_{\mathbf{0}}$ and $g_y = -\frac{q}{p_0}B_x|_{\mathbf{0}}$ where $\boldsymbol{B}$ is the magnetic field in the closed orbit basis. For example, $\boldsymbol{g}$ will be nonzero when the closed orbit through a quadrupole magnet is offset from the magnet centerline. Note that with this definition, $\boldsymbol{g}$ points in the opposite direction of $\hat{\boldsymbol{v}}$. The Thomas-BMT equation in this coordinate system is

$$\frac{d\boldsymbol{S}}{dt} = \boldsymbol{\Omega}_t \times \boldsymbol{S} \,,$$

$$\boldsymbol{\Omega}_t = -\frac{q}{p}v\left[(1+G\gamma)\boldsymbol{B} - G(\gamma-1)(\hat{\boldsymbol{\beta}}\cdot\boldsymbol{B})\hat{\boldsymbol{\beta}} + \left(G\gamma\beta + \frac{\gamma\beta}{1+\gamma}\right)\frac{\boldsymbol{E}\times\hat{\boldsymbol{\beta}}}{c}\right] - \frac{ds}{dt}\boldsymbol{g}\times\hat{\boldsymbol{s}} \,, \quad (5)$$

where $\boldsymbol{S}$ is a 3-vector of the spin expectation values in the closed orbit basis in the rest frame of the particle, G is the anomalous magnetic moment of the particle, and $\boldsymbol{B}$ and $\boldsymbol{E}$ are the laboratory frame magnetic and electric fields in the closed orbit basis [26, 7, 27, 11]. The $\boldsymbol{g}\times\hat{\boldsymbol{s}}$ term accounts for the rotation of the coordinate system. Expanding around the closed orbit (letting $\boldsymbol{r}_t = x\hat{\boldsymbol{x}} + y\hat{\boldsymbol{y}}$),

$$v \approx \frac{ds}{dt}\left(1 + \boldsymbol{g}\cdot\boldsymbol{r}_t\right) \,, \quad (6)$$

$$\frac{q}{p} \approx \frac{q}{p_0}(1-\delta) \,, \quad (7)$$

$$\gamma \approx \gamma_0(1+\beta_0^2\delta) \,, \quad (8)$$

$$\beta \approx \beta_0\left(1 + \delta/\gamma_0^2\right) \,, \quad (9)$$

$$\hat{\boldsymbol{\beta}} \approx (x'\hat{\boldsymbol{x}} + y'\hat{\boldsymbol{y}} + \hat{\boldsymbol{s}}) \,, \quad (10)$$

$$\boldsymbol{p} \approx p_0\left[x'\hat{x} + y'\hat{y} + (1+\delta)\hat{s}\right] \,. \quad (11)$$

Note that $\frac{ds}{dt}$ implicitly contains a δ dependence. Multiplying both sides of Eq. (5) by $\frac{dt}{ds}$ and substituting Eqs. (6) through (10), the Thomas-BMT equation can be rewritten as

$$\boldsymbol{S}' = \boldsymbol{\Omega}\times\boldsymbol{S} \quad (12)$$

where $\boldsymbol{\Omega} = \boldsymbol{\Omega}_B + \boldsymbol{\Omega}_E - \boldsymbol{g}\times\hat{\boldsymbol{s}}$ and

$$\Omega_{B,x} \approx -\frac{q}{p_0}\left\{\left[(1+G\gamma_0)(1+\boldsymbol{g}\cdot\boldsymbol{r}_t)-\left(1+\frac{G}{\gamma_0}\right)\delta\right]B_x+(G-G\gamma_0)x'B_s\right\}\,, \tag{13a}$$

$$\Omega_{B,y} \approx -\frac{q}{p_0}\left\{\left[(1+G\gamma_0)(1+\boldsymbol{g}\cdot\boldsymbol{r}_t)-\left(1+\frac{G}{\gamma_0}\right)\delta\right]B_y+(G-G\gamma_0)y'B_s\right\}\,, \tag{13b}$$

$$\Omega_{B,s} \approx -\frac{q}{p_0}\left\{(1+G)(1+\boldsymbol{g}\cdot\boldsymbol{r}_t-\delta)B_s+(G-G\gamma_0)(x'B_x+y'B_y)\right\}\,, \tag{13c}$$

$$\Omega_{E,x} \approx -\frac{q}{p_0}\left\{\left[G\beta_0\gamma_0+\frac{\beta_0\gamma_0}{1+\gamma_0}\right]\left[(1+\boldsymbol{g}\cdot\boldsymbol{r}_t)\frac{E_y}{c}-y'\frac{E_s}{c}\right]+\frac{\beta_0\gamma_0}{1+\gamma_0}\left[\frac{1}{\gamma_0}-1\right]\delta\frac{E_y}{c}\right\}\,, \tag{14a}$$

$$\Omega_{E,y} \approx -\frac{q}{p_0}\left\{\left[G\beta_0\gamma_0+\frac{\beta_0\gamma_0}{1+\gamma_0}\right]\left[x'\frac{E_s}{c}-(1+\boldsymbol{g}\cdot\boldsymbol{r}_t)\frac{E_x}{c}\right]+\frac{\beta_0\gamma_0}{1+\gamma_0}\left[1-\frac{1}{\gamma_0}\right]\delta\frac{E_x}{c}\right\}\,, \tag{14b}$$

$$\Omega_{E,s} \approx -\frac{q}{p_0}\left\{\left[G\beta_0\gamma_0+\frac{\beta_0\gamma_0}{1+\gamma_0}\right]\left[y'\frac{E_x}{c}-x'\frac{E_y}{c}\right]\right\}\,. \tag{14c}$$

We now consider only magnetostatic fields, expanded around the closed orbit to first-order. For convenience we define the quantities

$$K_s = \frac{q}{p_0}\,B_s|_{\mathbf{0}}\,, \tag{15}$$

$$K_1 = \frac{q}{p_0}\,\partial_y B_x\big|_{\mathbf{0}}\,, \tag{16}$$

$$\tilde{K}_1 = \frac{q}{2p_0}\left(\partial_x B_x|_{\mathbf{0}} - \partial_y B_y\big|_{\mathbf{0}}\right)\,. \tag{17}$$

In the special case where the closed orbit is aligned with the magnet centerlines, these quantities are equivalent to the normalized solenoid, quadrupole, and skew quadrupole strengths respectively. The general magnetic field satisfying the Maxwell equations $\boldsymbol{\nabla}\times\boldsymbol{B}=\boldsymbol{\nabla}\cdot\boldsymbol{B}=0$ to first-order is

$$B_x \approx -\frac{p_0}{q}\left(\frac{1}{2}K_s'x+g_y-K_1y+\tilde{K}_1x\right), \tag{18a}$$

$$B_y \approx -\frac{p_0}{q}\left(\frac{1}{2}K_s'y-g_x-K_1x-\tilde{K}_1y\right), \tag{18b}$$

$$B_s \approx -\frac{p_0}{q}\left(-K_s-g_x'y+g_y'x\right)\,. \tag{18c}$$

Substituting Eq. (18) into Eq. (13), we split $\boldsymbol{\Omega}$ into a zeroth order part $\boldsymbol{\Omega}_0$ on the closed orbit and a perturbative part $\boldsymbol{\omega}(\boldsymbol{\zeta})$ first-order in the phase space variables,

$$\Omega_{0,x} \approx G\gamma_0 g_y\,, \tag{19a}$$

$$\Omega_{0,y} \approx -G\gamma_0 g_x\,, \tag{19b}$$

$$\Omega_{0,s} \approx -(1+G)K_s\,, \tag{19c}$$

$$\omega_x \approx (1+G\gamma_0)\left(\frac{1}{2}K_s'x + g_y\boldsymbol{g}\cdot\boldsymbol{r}_t - K_1 y + \tilde{K}_1 x\right) + (G\gamma_0 - G)\,K_s x' - \left(1+\frac{G}{\gamma_0}\right)g_y\delta\,, \tag{20a}$$

$$\omega_y \approx (1+G\gamma_0)\left(\frac{1}{2}K_s'y - g_x\boldsymbol{g}\cdot\boldsymbol{r}_t - K_1 x - \tilde{K}_1 y\right) + (G\gamma_0 - G)\,K_s y' + \left(1+\frac{G}{\gamma_0}\right)g_x\delta\,, \tag{20b}$$

$$\omega_s \approx (1+G)\left(-K_s\boldsymbol{g}\cdot\boldsymbol{r_t} + K_s\delta - g_x'y + g_y'x\right) + (G\gamma_0 - G)\left(g_x y' - g_y x'\right)\,. \tag{20c}$$

Equivalent, alternative expressions for ω_x and ω_y can be obtained by substituting in the orbital equations of motion. Substituting Eqs. (6), (10), (11) and (18) into $\frac{d\boldsymbol{p}}{dt} = qv\hat{\boldsymbol{\beta}}\times\boldsymbol{B}$, we obtain

$$x'' - K_s y' - g_x\delta \approx \frac{1}{2}K_s'y - g_x\boldsymbol{g}\cdot\boldsymbol{r}_t - K_1 x - \tilde{K}_1 y\,, \tag{21}$$

$$-y'' - K_s x' + g_y\delta \approx \frac{1}{2}K_s'x + g_y\boldsymbol{g}\cdot\boldsymbol{r}_t - K_1 y + \tilde{K}_1 x\,. \tag{22}$$

Substituting Eq. (21) into Eq. (20b) and Eq. (22) into Eq. (20a) gives

$$\omega_x \approx -(1+G\gamma_0)\,y'' - (1+G)\,K_s x' + \left(G\gamma_0 - \frac{G}{\gamma_0}\right)g_y\delta\,, \tag{23a}$$

$$\omega_y \approx (1+G\gamma_0)\,x'' - (1+G)\,K_s y' - \left(G\gamma_0 - \frac{G}{\gamma_0}\right)g_x\delta\,. \tag{23b}$$

1.3 Strong Synchrobeta Spin Matching

To minimize the effects of radiative depolarization, a *strong synchrobeta spin match* should first be applied [6, 8]: the magnet strengths and spin rotator configuration are chosen so that the 1-turn spin dependence on the orbit motion is removed at as many azimuths as possible. By minimizing the 1-turn spin-orbit coupling where photons are emitted, $\boldsymbol{d}$ is also minimized. This is usually done to first-order in the phase space coordinates' deviation from the closed orbit. To do so, we first construct a right-handed orthonormal coordinate system $(\hat{\boldsymbol{n}}_0, \hat{\boldsymbol{m}}_0, \hat{\boldsymbol{l}}_0)$ where $\hat{\boldsymbol{l}}_0$ and $\hat{\boldsymbol{m}}_0$ solve the Thomas-BMT equation along the closed orbit. Note that this coordinate system is not 1-turn periodic, with $\hat{\boldsymbol{m}}_0$ and $\hat{\boldsymbol{l}}_0$ having precessed by the closed orbit spin tune ν_0 around $\hat{\boldsymbol{n}}_0$ after one turn. We can approximate any particle's spin for small deviations from $\hat{\boldsymbol{n}}_0$ as

$$\boldsymbol{S} \approx \hat{\boldsymbol{n}}_0 + \kappa_1\hat{\boldsymbol{m}}_0 + \kappa_2\hat{\boldsymbol{l}}_0\,, \tag{24}$$

to first-order in κ_1 and κ_2. Substituting Eq. (24) into Eq. (12), we obtain

$$\frac{d\kappa_1}{ds} \approx \boldsymbol{\omega}(\zeta)\cdot\hat{\boldsymbol{l}}_0\,,\ \frac{d\kappa_2}{ds} \approx -\boldsymbol{\omega}(\zeta)\cdot\hat{\boldsymbol{m}}_0\,. \tag{25}$$

Defining $\boldsymbol{k}_0 = \hat{\boldsymbol{l}}_0 - \mathrm{i}\hat{\boldsymbol{m}}_0$, the first-order 1-turn spin-orbit coupling at some position s_0 is removed when

$$\int_{s_0}^{s_0+C} \boldsymbol{\omega}(\zeta) \cdot \boldsymbol{k}_0 \, ds = 0 \,, \tag{26}$$

where C is the total length of the closed orbit. Which ζ should we evaluate Eq. (26) for? We can express any ζ as a linear combination of the linear compositional map eigenvectors $\boldsymbol{v}_i$ in each plane $i = \pm I, \pm II, \pm III$. In a weakly-coupled ring, satisfying Eq. (26) with $\zeta = \boldsymbol{v}_{\pm I}$ would be referred to as a "horizontal strong synchrobeta spin match".

1.4 Harmonic Closed Orbit Spin Matching

In real rings, random closed orbit distortions will, generally, reduce the polarization further. In HERA, *harmonic closed orbit spin matching* (HCOSM) was employed to correct this additional depolarization [5, 4]. HCOSM focuses on correcting the tilt of $\hat{\boldsymbol{n}}_0$ from its design direction caused by the random errors, by using vertical orbit bumps that optimally cancel the integer Fourier harmonics of the tilt precession nearest to ν_0. To quantify the tilt, a 1-turn periodic orthonormal coordinate system $(\hat{\boldsymbol{n}}_0, \hat{\boldsymbol{m}}, \hat{\boldsymbol{l}})$ is constructed in the *ideal* ring where

$$\hat{\boldsymbol{m}}(s) + \mathrm{i}\hat{\boldsymbol{l}}(s) = e^{-\mathrm{i}\psi(s)} \left(\hat{\boldsymbol{l}}_0(s) + \mathrm{i}\hat{\boldsymbol{m}}_0(s) \right) \,, \tag{27}$$

and $\psi(s)$ is the so-called spin phasing function which must be chosen so that $\psi(s_0 + C) - \psi(s_0) = 2\pi\nu_0$ for 1-turn periodicity. For HERA, the spin phasing function was chosen to linearly evolve with s so that

$$\psi(s) = \psi(s_0) + 2\pi\nu_0 \frac{s - s_0}{C} \,. \tag{28}$$

Assuming small closed orbit perturbations, various vertical orbit bumps in the ring are turned on and the original unperturbed $\hat{\boldsymbol{l}}$ and $\hat{\boldsymbol{m}}$ are attached to the new perturbed closed orbits. A Fourier transform of the projections of the new $\hat{\boldsymbol{n}}_0$ on $\hat{\boldsymbol{l}}$ and $\hat{\boldsymbol{m}}$ for each bump can then be taken, and each bump's impact on the integer harmonics nearest to ν_0 can be calculated. Finally, groups of the bumps are formed *ab initio* to construct special bumps that ideally only impact a single integer harmonic of the $\hat{\boldsymbol{n}}_0$ tilt along $\hat{\boldsymbol{l}}$ or $\hat{\boldsymbol{m}}$. These bumps are then varied to correct the depolarization caused by random closed orbit distortions.

While HCOSM did prove effective for HERA, it suffers from various disadvantages. Firstly, HCOSM of course is only intended to be applied for correcting the depolarization in a ring with random closed orbit distortions, not for increasing polarization in the ideal ring. Secondly, HCOSM indirectly attacks the real problem, which is $\boldsymbol{d}$: it assumes that tilts to $\hat{\boldsymbol{n}}_0$ are always bad, and that bumps that maximally impact the integer spin harmonics nearest to ν_0 will optimally correct the tilt and optimally impact $\boldsymbol{d}$. Thirdly, HCOSM as applied in HERA provided no systematic way of dealing with the spurious vertical dispersion created by the bumps, and coupling if there are sextupoles

between the corrector coils in a bump. Fourthly, HCOSM does not ensure minimal orbit excursions for a maximum impact on the Fourier harmonics. A new more powerful method called Best Adjustment Groups for ELectron Spin, introduced in Sec. 4, does not have any of these setbacks, and is preferred for correcting polarization in operation.

1.5 Computational Methods

Computation of Eqs. (1), (3), and (4) directly can be costly, and some useful approximations may be made to speed up the calculation and obtain a reasonable estimate. Firstly, instead of averaging over the ensemble, we can approximate by evaluating the integral only on the closed orbit, i.e. $\hat{\boldsymbol{n}} \approx \hat{\boldsymbol{n}}_0$, $\boldsymbol{d} \approx \boldsymbol{d}(\boldsymbol{0})$, $\hat{\boldsymbol{\beta}} \approx \hat{\boldsymbol{\beta}}(\boldsymbol{0})$, $\hat{\boldsymbol{v}} \approx \hat{\boldsymbol{v}}(\boldsymbol{0})$, and $\dot{\hat{\boldsymbol{v}}} \approx \dot{\hat{\boldsymbol{v}}}(\boldsymbol{0})$. Secondly, using Eqs. (8) and (9) it is easy to show that in the ultra relativistic case $\boldsymbol{d}(\boldsymbol{0}) = \gamma_0 \frac{\partial \hat{\boldsymbol{n}}}{\partial \gamma}\Big|_{\boldsymbol{0}} = \frac{\partial \hat{\boldsymbol{n}}}{\partial \delta}\Big|_{\boldsymbol{0}}$. This term can be easily extracted as a coefficient in the first-order truncated power series expansion of $\hat{\boldsymbol{n}}$ around the closed orbit.

These approximations give a generally excellent estimate for the Sokolov-Ternov terms (those NOT $\propto \boldsymbol{d}$). However, $\boldsymbol{d}$ can vary significantly even with small variations from the closed orbit. Nonlinearities in the orbital motion that excite a larger beam size may exacerbate the problem. Therefore, to accurately estimate the effects of radiative depolarization, nonlinear Monte Carlo spin tracking including radiation damping and radiation fluctuations is necessary. In such tracking spin-flip effects should be excluded and the initial beam distribution should be in radiative equilibrium. Then, τ_{dep} can be obtained directly from the slope of P vs. t, and P_{dk} can be approximated as

$$P_{dk} \approx P_{st} \frac{\tau_{st}^{-1}}{\tau_{st}^{-1} + \tau_{dep}^{-1}} , \tag{29}$$

where P_{st} is just P_{dk} with $\boldsymbol{d} = \boldsymbol{0}$.

In this dissertation, we will refer to the approximation $\boldsymbol{d} \approx \boldsymbol{d}(\boldsymbol{z}_{\text{c.o.}})$ as the *analytical* calculation because with this approximation the DK integral can be calculated quickly without tracking.

2 Electron-Ion Collider: Electron Storage Ring (ESR)

2.1 Overview

The ESR will provide longitudinally-polarized electron bunches at each of roughly 5, 10, and 18 GeV in both a 1- and 2-colliding interaction point (IP) configuration using the spin rotator shown in Fig. 2. The spin rotator of the ESR, consists of a symmetric arrangement of four solenoid modules and four bend modules around the IP [13]. Each "solenoid module" consists of two half solenoids, separated by either 5 (short) or 7 (long) quadrupoles with strengths chosen for decoupling and spin matching, as shown in Fig. 3. See Sec. 2.3 for a description

of the minimal number of quadrupoles in each module needed to achieve both decoupling and spin matching. For each energy (which defines the bend spin precession ψ_j), the solenoid strengths ϕ_i are set for longitudinal spin at the IP. The spin rotator configuration was chosen so that at roughly 5 GeV, only the short solenoid modules are turned on, and at roughly 18 GeV, only the long solenoid modules are turned on (Table 1). In these two cases, the "on" solenoid module rotates $\hat{\boldsymbol{n}}_0$ from the vertical to the horizontal, and the bend module(s) (where spin precession is proportional to γ_0) rotates $\hat{\boldsymbol{n}}_0$ from the horizontal to the longitudinal. For the 10 GeV case, all solenoid modules must be used.

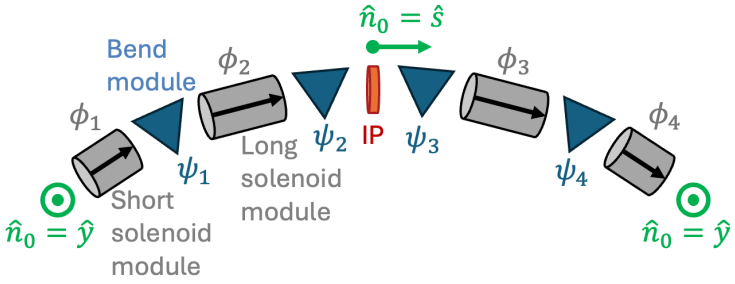

Figure 2: Top-down view of the spin rotator of the ESR, with the spin precession angles in each module labelled.

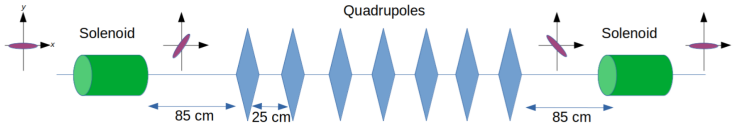

Figure 3: "Solenoid modules" consist of two half-solenoids separated by either 5 or 7 quadrupoles for decoupling and spin matching [14].

Table 1: Solenoid ($\hat{s}$) and bend ($\hat{y}$) module spin precession angles at different energies using the right-handed basis ($\hat{x}, \hat{y}, \hat{s}$) with $\hat{s}$ pointing along the longitudinal in Fig. 2

	Solenoids		**Bends**	
	$\phi_{1,4}$	$\phi_{2,3}$	$\psi_{1,4}$	$\psi_{2,3}$
17.846 GeV 1-IP/2-IP	0°	−90°	N/A	−90°
9.781 GeV 1-IP	−52.2°	−126.0°	−124.4°	−49.3°
9.650 GeV 2-IP	−51.7°	−124.4°	−122.7°	−48.7°
5.068 GeV 1-IP/2-IP	−90°	0°	−64.4°	−25.6°

To avoid depolarizing integer spin resonances, the exact operating energies

are those closest to 5, 10, and 18 GeV that give a half-integer fractional closed-orbit spin tune ν_0. At 5 and 18 GeV, because of the special rotator configuration chosen, the "net" spin precession of $\hat{\boldsymbol{l}}_0$ and $\hat{\boldsymbol{m}}_0$ across the rotator is exactly equal to 180°; in these special cases, the contribution to ν_0 of the rotator is equivalent to that with the rotator been turned off. Therefore, for 5 and 18 GeV, $\nu_0 = a\gamma_0$, and there is no difference in the energies of the 1-IP and 2-IP lattices. The 10 GeV lattice does not have this special configuration, and so there is a small difference in the energy (and solenoid settings) between the 1-IP and 2-IP lattices to maintain a half-integer ν_0; numerical solution was required to calculate the exact γ_0's closest to 10 GeV.

2.2 Polarization Figures-Of-Merit

Helicity is the projection of a particle's spin onto the direction of its momentum, with a positive helicity corresponding to the spin pointing along the momentum and a negative helicity corresponding to the spin pointing opposite the momentum. In HERA, all bunches had the same helicities at the IP. Unpolarized bunches were injected and self-polarized using the Sokolov-Ternov effect, up to the asymptotic polarization P_{dk}. Therefore, after self-polarization, P_{dk} quantified the time-averaged polarization at the IP, and was a good polarization figure-of-merit for HERA.

In the EIC-ESR, bunches with both positive and negative helicities at the IP(s) will be stored simultaneously, in order to minimize systematic errors in the collisions [1]. This can be achieved by having two types of bunches circulating at the same time in the ring: bunches with polarizations pointing antiparallel to the arc fields (outside the rotator), and bunches with polarizations pointing parallel to the arc fields. Per Fig. 2, we see that, for electrons, the antiparallel-polarized bunches (with polarizations pointing in the $+\hat{\boldsymbol{y}}$ direction outside the rotator) have positive helicity at the IP, and the parallel-polarized bunches (with polarizations pointing in the $-\hat{\boldsymbol{y}}$ direction outside the rotator) have negative helicity at the IP. For this case, we cannot simply inject unpolarized bunches and use the Sokolov-Ternov effect to build up polarization, because all bunches will have polarizations building up along the same direction. Instead, we must inject *polarized* bunches with the correct directions for positive/negative helicities, and swap-out each bunch once sufficiently depolarized with a fresh, polarized bunch. However, the Sokolov-Ternov effect will work *against* the parallel-polarized bunches, and *for* the antiparallel-polarized bunches. Therefore, in order to maintain a sufficient time averaged polarization for each bunch type at the IP(s), the parallel-polarized bunch replacement time T_- must be less than the antiparallel-polarized bunch replacement time T_+.

For the EIC-ESR, we require that a time-averaged polarization of $|\langle P \rangle_t| \geq 70\%$ is maintained. The time-averaged polarizations for antiparallel-polarized

bunches and parallel-polarized bunches are respectively

$$\langle P_+\rangle_t = \frac{1}{T_+}\int_0^{T_+} P(P_0^+;t)\,dt\,, \quad \langle P_-\rangle_t = \frac{1}{T_-}\int_0^{T_-} P(P_0^-;t)\,dt\,, \tag{30}$$

where P_0^+ is the initial antiparallel-polarized bunch polarization at injection, and likewise P_0^- for the parallel-polarized bunch. The polarization time evolution is defined in Eq. (2). In all studies presented in this dissertation, we assume that $P_0^+ = -P_0^- = P_0 = 85\%$, where we choose the convention that antiparallel polarization is positive [28]. Furthermore, we also require that $\langle P_+\rangle_t = -\langle P_-\rangle_t = \langle P\rangle_t \geq 70\%$. Performing the integrations in Eq. (30) we have

$$\langle P_\pm\rangle_t = \pm\langle P\rangle_t = P_{dk} - \frac{\tau_{dk}}{T_\pm}\left(P_{dk} \mp P_0\right)\left(1 - e^{-T_\pm/\tau_{dk}}\right)\,. \tag{31}$$

We can solve for $T_\pm$, obtaining

$$T_\pm = \tau_{eq}\left[\tilde{P}_\pm + W_k(-\tilde{P}_\pm e^{-\tilde{P}_\pm})\right]\,,\ \tilde{P}_\pm = \frac{P_{dk} \mp P_0}{P_{dk} \mp \langle P\rangle_t} \tag{32}$$

where W_k is the k-th branch of the Lambert W function. Because $T_\pm$ must be real, we have the $k = 0$ branch which covers the domain $[-1/e, \infty)$ and the $k = -1$ branch which covers the domain $[-1/e, 0)$. To determine which branch, consider the identities

$$W_0(-xe^{-x}) = -x \quad \text{for } x \leq 1\,, \tag{33}$$

$$W_{-1}(-xe^{-x}) = -x \quad \text{for } x \geq 1\,. \tag{34}$$

Considering Eq. (32), we see that if W_0 is used when $\tilde{P}_\pm \leq 1$, or if W_{-1} is used when $\tilde{P}_\pm \geq 1$, then we have a trivial solution $T_\pm = 0$, which we do not want. Let's consider the form of $\tilde{P}_\pm$ in Eq. (32), where we defined P_0, P_{dk}, and $\langle P\rangle_t$ as solely positive quantities. Note that if $\langle P\rangle_t \geq P_{dk}$, then we must have $P_0 \geq \langle P\rangle_t$ else the requirement that $\langle P_+\rangle_t = \langle P\rangle_t$ is unachievable, because the positive polarization will decay to P_{dk}. Alternatively, if we have $\langle P\rangle_t \leq P_{dk}$, then there is *no possible* P_0 such that $P_0^+ = -P_0^- = P_0$ to achieve $\langle P_-\rangle_t = -\langle P\rangle_t$, as the negative polarization will only decrease from P_0. Therefore, in order to maintain symmetry for ech type of bunch in the ESR, we can only have $\langle P\rangle_t \geq P_{dk}$ and therefore $P_0 \geq \langle P\rangle_t$. With such conditions, per Eq. (32) we see that $\tilde{P}_\pm \geq 1$. Therefore, we must use the $k = 0$ branch of the Lambert W function. This leaves us with

$$T_\pm = \tau_{dk}\left[\tilde{P}_\pm + W_0(-\tilde{P}_\pm e^{-\tilde{P}_\pm})\right]\,. \tag{35}$$

At the time of this dissertation-writing, the Rapid Cycling Synchrotron (RCS), shown in Fig. 1, is planned to replace bunches in the ESR with a maximal rate of $f_{RCS,max} = 1$ bunch/second. Using this rate, there are two good figures-of-merit we will use to quantity the polarization performance in the ESR.

The first figure-of-merit corresponds to the bunch replacement times necessary to maintain a time-averaged polarization of exactly $\langle P\rangle_t = 70\%$. Specifically, we solve for $T_\pm$ in Eq. (35) where $\langle P\rangle_t = 70\%$. With these T_- and T_+

consider that at any given time the EIC-ESR must have N bunches circulating in the ring, N_+ of which have antiparallel polarization and N_- having parallel polarization. We require that $N_+ = N_- = N/2$. At 5 and 10 GeV, $N = 1160$, and at 18 GeV, $N = 290$. In order to maintain sufficient polarization, each of the N_+ bunches must be replaced every T_+ minutes, therefore requiring an average bunch replacement rate of N_+/T_+ for the (+) bunches. Likewise, each of the N_- bunches must be replaced every T_- minutes, therefore requiring an average bunch replacement rate of N_-/T_- for the (−) bunches. Using the fact that $N_+ = N_- = N/2$, for some long time t the total number of bunches replaced N_{tot} to maintain sufficient polarization is

$$N_{tot}(t) = \frac{N}{2}\left(\frac{1}{T_+} + \frac{1}{T_-}\right)t \ . \tag{36}$$

This must be ≤ the number of bunches the RCS can possibly replace in that same time,

$$\frac{N}{2}\left(\frac{1}{T_+} + \frac{1}{T_-}\right) \leq f_{RCS,max} \ . \tag{37}$$

Both sides of Eq. (37) correspond to rates in bunches/time. With some minor massaging of this inequality, we can obtain the requirement in units of time to replace N bunches specifically,

$$T \geq \frac{N}{f_{RCS,max}} \ , \quad T = \frac{2T_-T_+}{T_- + T_+} \ . \tag{38}$$

The T in Eq. (38) is the first figure-of-merit we use to quantify polarization in the ESR. Note that the N bunches replaced in these times do NOT necessarily correspond to $N/2$ antiparallel-polarized bunches and $N/2$ parallel-polarized bunches, rather just N bunches. E.g., because $T_- < T_+$, then N consists of more (−) than (+) bunches. The reason why T is used instead of T/N throughout this dissertation is simply a matter of convenience: this figure-of-merit is independent of the number of bunches stored in the ring, which instead defines the minimum allowed amount. This figure-of-merit T we refer to as the *N bunch replacement time*.

The second figure-of-merit is computed differently; now, we consider what possible time-averaged polarization is achieved assuming that the RCS replaces the bunches with its maximum possible rate of $f_{RCS,max}$. Setting $\langle P_+\rangle_t = -\langle P_-\rangle_t$, we have two unknowns T_- and T_+. Letting the T in Eq. (38) equal $N/f_{RCS,max}$, we can connect T_- to T_+ and get an equation with only one unknown. This can be solved for numerically, and we can then obtain the $\langle P\rangle_t$ achievable. Of course, once $\langle P\rangle_t = P_{dk}$, then the (+) bunches are never replaced, i.e. $T_+ \to \infty$, and all of the bunches replaced by the RCS are (−) bunches. Therefore, if we maintain the symmetry requirement that $\langle P_+\rangle_t = -\langle P_-\rangle_t$, then no further improvements to polarization can be made beyond this point. Per Eq. (38), when $T_+ \to \infty$, $T_- \to T/2$.

In this work, we use both of these figures-of-merit. It is insightful to consider how T, T_-, T_+, and $\langle P\rangle_t$ are related to P_{dk}. To do so, we use the following approximations: (i) those described at the beginning of Sec. 1.5, (ii)

Eq. (29) which neglects kinetic effects, and (iii) neglect changes to τ_{st} and P_{st} with changes to τ_{dep} – this is reasonable by observation of Eq. (3) and Eq. (1), where we see that if the closed orbit and $\hat{n}_0$ are approximately unchanged, then these quantities (in their current approximations) will not change. With these approximations, we can numerically compute relations of T and $\langle P \rangle_t$ with P_{dk}. Figures 4 and 5 show the relation of T and $\langle P \rangle_t$ vs. P_{dk} for the 18 GeV 1-IP ESR respectively. For this lattice, $P_{st} = 86.7\%$, $\tau_{st} = 36.3$ min, and $N = 290$. Given the RCS's maximum replacement rate of 60 bunches/second we require $T \geq 4.8$ min per Eq. (38). For $\langle P \rangle_t$, we simply require $\langle P \rangle_t \geq 70\%$. Both of these figures may be useful in interpreting the plots presented throughout this dissertation.

2.3 Strong Synchrobeta Spin Match

The ESR satisfies a horizontal strong synchrobeta spin match everywhere outside of the spin rotator for each energy case. A vertical strong synchrobeta spin match is not feasible due to its complexity. At 5 and 10 GeV the effects

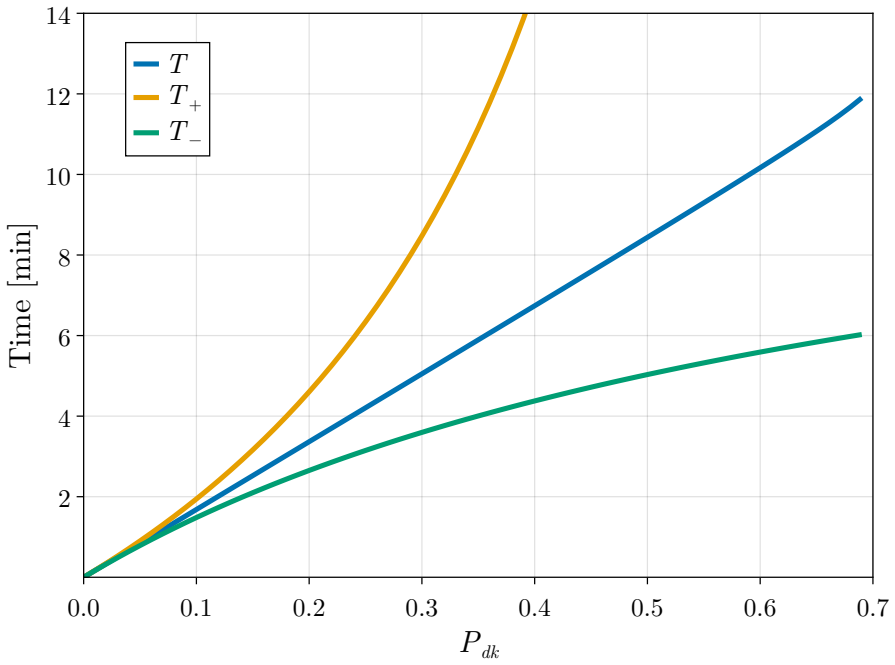

Figure 4: N bunch replacement time T, (defined in Eq. (38)), T_+, and T_- vs. P_{dk} for the 1-IP 18 GeV EIC-ESR in order to maintain a time averaged polarization of 70%. This lattice has $P_{st} = 86.7\%$, and $\tau_{st} = 36.3$ min. T must be ≥ 4.8 min, which is the minimal N bunch replacement time achievable by the RCS.

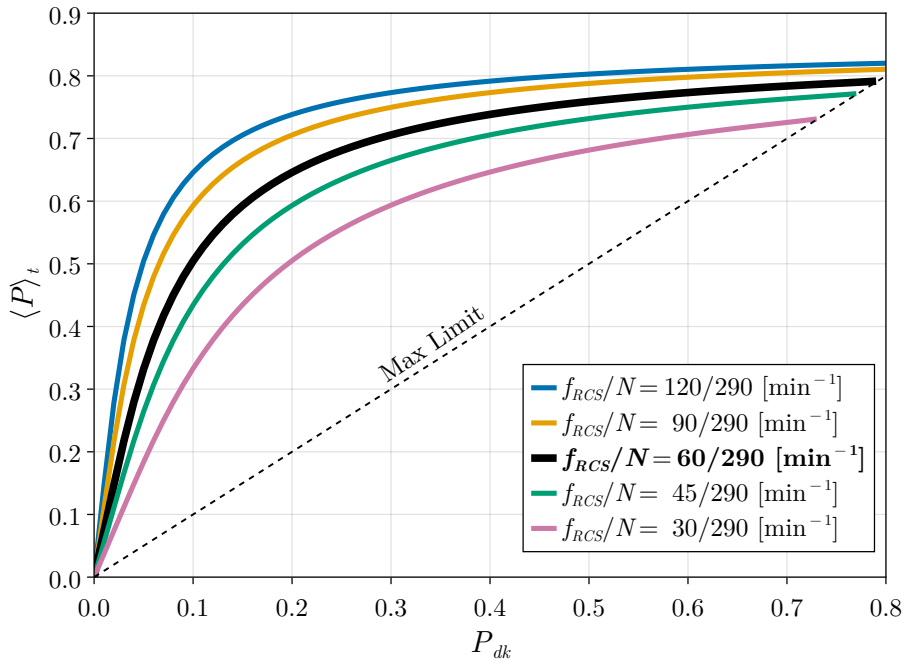

Figure 5: Time-averaged polarization achieved for both parallel- and antiparallel-polarized bunches $\langle P \rangle_t$ vs P_{dk} in the 18 GeV 1-IP EIC-ESR, assuming N bunches in the ring and a bunch replacement rate of f_{RCS}. The bold entry corresponds to the planned value for the EIC-ESR.

of synchrotron radiation make a longitudinal strong synchrobeta spin match not necessary, but at 18 GeV the effect is significant. Early versions of the 18 GeV EIC-ESR had a longitudinal strong synchrobeta spin match, however this later had to be dropped because it required either 11 Tesla solenoids or geometry changes to the current RHIC tunnel, both of which are infeasible. The lack of a longitudinal spin match has severe consequences on the polarization at 18 GeV; Figure 6 shows the difference in the N bunch replacement time between an early 1-IP ESR version that had a longitudinal spin match (LSM) vs. a later one where the LSM was dropped. Chapter 3 shows an attempt to resolve this problem via a "partial" longitudinal spin match, and Sec. 4 shows a novel approach that not only solves this problem, but also provides a solution for general simultaneous control of the orbit, optics, and polarization in electron rings. The spin matching conditions for the EIC-ESR, derived by V. Ptitsyn [16], are now re-derived in detail to a simple general form [21]. Evaluating the integrand in Eq. (26) using Eqs. (23a), (23b), and (20c) for the EIC-ESR spin rotator

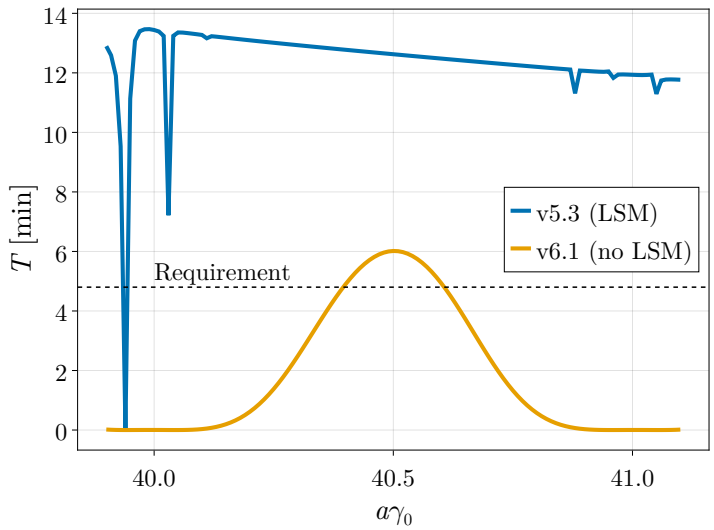

Figure 6: Energy scan of the N bunch replacement time for two versions of the 1-IP 18 GeV EIC-ESR, one which has a longitudinal spin match (LSM) and one without an LSM.

gives

$$\begin{aligned}\boldsymbol{\omega}\cdot\boldsymbol{k}_0 &= K_s\left[-(1+a)(x'k_{0,x}+y'k_{0,y}-\delta k_{0,s})\right]+g_x\left[(a\gamma_0-a)y'k_{0,s}-\left(a\gamma_0-\frac{a}{\gamma_0}\right)\delta k_{0,y}\right]\\ &\quad -g_x'(1+a)yk_{0,s}+(1+a\gamma_0)(x''k_{0,y}-y''k_{0,x})\\ &= K_s\left[-(1+a)(x'k_{0,x}+y'k_{0,y}-\delta k_{0,s})\right]+g_x\left[(a\gamma_0-a)y'k_{0,s}-\left(a\gamma_0-\frac{a}{\gamma_0}\right)\delta k_{0,y}\right]\\ &\quad -g_x'(1+a)yk_{0,s}+(1+a\gamma_0)\left[(x'k_{0,y})'-x'k_{0,y}'-(y'k_{0,x})'+y'k_{0,x}'\right],\end{aligned} \tag{39}$$

where the convention for electrons $G\to a$ is used. Substitution of $\boldsymbol{k}_0$ into $\boldsymbol{S}'=\boldsymbol{\Omega}_0\times\boldsymbol{S}$ using Eq. (19) gives

$$k_{0,x}' = (1+a)K_sk_{0,y}-a\gamma_0g_xk_{0,s}\,, \tag{40a}$$
$$k_{0,y}' = -(1+a)K_sk_{0,x}\,, \tag{40b}$$
$$k_{0,s}' = a\gamma_0g_xk_{0,x}\,. \tag{40c}$$

With these equations, the integrand is

$$\begin{aligned}\boldsymbol{\omega}\cdot\boldsymbol{k}_0 &= K_s(1+a)\left[a\gamma_0\left(x'k_{0,x}+y'k_{0,y}\right)+\delta k_{0,s}\right]-g_x\left[(a+a^2\gamma_0^2)y'k_{0,s}+\left(a\gamma_0-\frac{a}{\gamma_0}\right)\delta k_{0,y}\right]\\ &\quad -g_x'(1+a)yk_{0,s}+(1+a\gamma_0)\left[(x'k_{0,y})'-(y'k_{0,x})'\right]\,.\end{aligned} \tag{41}$$

2.3.1 Horizontal Spin Match

We now substitute $\boldsymbol{\zeta} = \boldsymbol{v}_I$, the horizontal-like eigenvector, into Eq. (41). With this substitution, the integrals over the $(y'k_{0,x})'$ and $(x'k_{0,y})'$ terms are automatically zero: at the start and exit of the spin rotator we demand no transverse coupling, so $v_{I,p_y}(s_{in}) = v_{I,p_y}(s_{out}) = 0$, and $\hat{\boldsymbol{n}}_0$ is vertical, so $k_{0,y}(s_{in}) = k_{0,y}(s_{out}) = 0$. Furthermore, because there is no transverse coupling in the bends, $v_{I,y} = v_{I,p_y} = 0$ in the bends. Finally, $v_{I,\delta} = 0$. This leaves integrals only over the eight solenoids (two per solenoid module). Using the fact that $x' = p_x + \frac{1}{2}K_s y$ and $y' = p_y - \frac{1}{2}K_s x$, this is expressed in terms of the canonical components of $\boldsymbol{v}_I$ as

$$\int_{s_{in}}^{s_{out}} \boldsymbol{\omega} \cdot \boldsymbol{k}_0 \, ds = \int_{8\text{ sols}} K_s(1+a)a\gamma_0 \left[\left(v_{I,p_x} + \frac{1}{2}K_s v_{I,y} \right) k_{0,x} + \left(v_{I,p_y} - \frac{1}{2}K_s v_{I,x} \right) k_{0,y} \right] ds \, . \tag{42}$$

Solving the equations of motion in Eq. (21) and Eq. (22) for a solenoid shows that x' and y' rotate together at a rate of K_s radians per unit length. Likewise, solving the equations of motion in Eq. (40a) and Eq. (40b) for a solenoid shows that the transverse spin components $k_{0,x}$ and $k_{0,y}$ rotate and at a rate of $(1+a)K_s$ radians per unit length. For electrons, $a \approx 0.00116$. In the ESR spin matching conditions derivation, it is assumed that a is sufficiently small so that $(1+a) \approx 1$. With this assumption, the spin and velocity precess at approximately the same rate, and so $\left(x'k_{0,x} + y'k_{0,y}\right)$ is constant within each solenoid. Letting L be the length of an individual solenoid, this leaves a sum over each of the eight solenoids in the rotator,

$$a\gamma_0 \sum_{j=1}^{8\text{ sols}} (K_s L)_j \left[\left(v_{I,p_x} + \frac{1}{2}K_s v_{I,y} \right) k_{0,x} + \left(v_{I,p_y} - \frac{1}{2}K_s v_{I,x} \right) k_{0,y} \right]_j = 0 \, . \tag{43}$$

Because the summand is constant within a single solenoid, it can be evaluated at the start, end, or anywhere in between inside that single solenoid. Once again, there are four solenoid modules each consisting of two equal strength solenoids with equal length L. It is convenient to express the spin matching conditions in terms of each solenoid module (each consecutive pair of single solenoids), because we can evaluate the summand right at the start of the first solenoid entering the module, and at the end of the second solenoid exiting the module. With the spin precession through the entire i-th solenoid module as $\phi_i = -2(K_s L)_i(1+a) \approx -2(K_s L)_i$, we express the horizontal spin matching conditions as

$$a\gamma_0 \sum_{i=1}^{4} H_i = 0 \, , \tag{44}$$

$$\begin{aligned} H_i = -\frac{\phi_i}{2} \Bigg\{ & \left[\left(v_{I,p_x} + \frac{1}{2}K_s v_{I,y} \right) k_{0,x} + \left(v_{I,p_y} - \frac{1}{2}K_s v_{I,x} \right) k_{0,y} \right]_{enter} \\ & + \left[\left(v_{I,p_x} + \frac{1}{2}K_s v_{I,y} \right) k_{0,x} + \left(v_{I,p_y} - \frac{1}{2}K_s v_{I,x} \right) k_{0,y} \right]_{exit} \Bigg\}_i \, . \end{aligned} \tag{45}$$

$(\boldsymbol{v}_I)_{exit}$ can be expressed in terms of $(\boldsymbol{v}_I)_{enter}$ multiplied by the orbital transfer matrix over the i-th solenoid module, and $(\boldsymbol{k}_0)_{exit}$ can be expressed in terms of $(\boldsymbol{k}_0)_{enter}$ multiplied by the spin rotation matrix over the solenoid module. Furthermore, there is no coupling entering and exiting each solenoid module, and so $\left(v_{I,y}\right)_{enter} = \left(v_{I,p_y}\right)_{enter} = \left(v_{I,y}\right)_{exit} = \left(v_{I,p_y}\right)_{exit} = 0$. Explicitly,

$$(v_{I,x})_{exit} = (v_{I,x})_{enter} m_{11} + (v_{I,p_x})_{enter} m_{12} \,, \tag{46}$$

$$(v_{I,p_x})_{exit} = (v_{I,x})_{enter} m_{21} + (v_{I,p_x})_{enter} m_{22} \,, \tag{47}$$

$$(k_{0,x})_{exit} = (k_{0,x})_{enter} \cos\phi_i - (k_{0,y})_{enter} \sin\phi_i \,, \tag{48}$$

$$(k_{0,y})_{exit} = (k_{0,x})_{enter} \sin\phi_i + (k_{0,y})_{enter} \cos\phi_i \,. \tag{49}$$

Thus,

$$H_i = \frac{\phi_i}{2} \left\{ v_{I,p_x} \left[k_{0,x} \left(1 + m_{22} \cos\phi_i + m_{12} \frac{1}{2} K_s \sin\phi_i \right) + k_{0,y} \left(m_{22} \sin\phi_i - m_{12} \frac{1}{2} K_s \cos\phi_i \right) \right] \right.$$
$$\left. v_{I,x} \left[k_{0,x} \left(m_{21} \cos\phi_i + m_{11} \frac{1}{2} K_s \sin\phi_i \right) + k_{0,y} \left(-\frac{1}{2} K_s + m_{21} \sin\phi_i - m_{11} \frac{1}{2} K_s \cos\phi_i \right) \right] \right\}_{enter} . \tag{50}$$

The horizontal spin matching conditions can be satisfied by setting H_i for each solenoid module such that the sum in Eq. (44) is equal to zero. One way of doing this is setting each $H_i = 0$. We also seek a solution which does not depend on the incoming eigenvector. The goal therefore is to choose the transfer matrix components over the solenoid module so that the terms proportional to $v_{I,x}$ and proportional to v_{I,p_x} are each zero. First, we consider the solution which is independent of the incoming $\boldsymbol{k}_0$, such that each term proportional to the components of $\boldsymbol{k}_0$ is zero. Solving the system for m_{22} and m_{12} (proportional to v_{I,p_x} and for m_{21} and m_{11} (proportional to $v_{I,x}$), and taking care to never divide by $\cos\phi_i$ which will equal zero when $\phi_i = 90°$, gives the transfer matrix elements for an arbitrary incoming $\boldsymbol{k}_0$, the so-called *universal solution*,

$$\mathsf{M}_{i,x} = \begin{pmatrix} -\cos\phi_i & -\frac{2}{K_s} \sin\phi_i \\ \frac{K_s}{2} \sin\phi_i & -\cos\phi_i \end{pmatrix} . \tag{51}$$

It seems, by coincidence, that the universal solution satisfies the symplectic condition $\det(\mathsf{M}) = 1$. Now, we consider possible other solutions dependent on the incoming $\boldsymbol{k}_0$. From this point forward, we will omit the subscript *enter* and assume it is implied. We rewrite Eq. (50) as

$$H_i = \frac{\phi_i}{2} \left\{ v_{I,p_x} \left[m_{22} \left(k_{0,x} \cos\phi_i + k_{0,y} \sin\phi_i \right) + m_{12} \left(k_{0,x} \frac{1}{2} K_s \sin\phi_i - k_{0,y} \frac{1}{2} K_s \cos\phi_i \right) + k_{0,x} \right] \right.$$
$$\left. v_{I,x} \left[m_{21} \left(k_{0,x} \cos\phi_i + k_{0,y} \sin\phi_i \right) + m_{11} \left(k_{0,x} \frac{1}{2} K_s \sin\phi_i - k_{0,y} \frac{1}{2} K_s \cos\phi_i \right) - \frac{1}{2} K_s k_{0,y} \right] \right\} . \tag{52}$$

Let

$$A = k_{0,x}\cos\phi_i + k_{0,y}\sin\phi_i \ , \tag{53}$$

$$B = k_{0,x}\frac{1}{2}K_s\sin\phi_i - k_{0,y}\frac{1}{2}K_s\cos\phi_i \ . \tag{54}$$

The spin matching conditions for any incoming $\boldsymbol{k}_0$ can be written as

$$Am_{22} + Bm_{12} = -k_{0,x} \ , \tag{55}$$

$$Am_{21} + Bm_{11} = \frac{1}{2}K_s k_{0,y} \ . \tag{56}$$

Including the symplectic condition, we calculate $m_{11}\times$(Eq. (55)) $- m_{12}\times$(Eq. (56)) to be

$$\begin{aligned} A\left(m_{11}m_{22} - m_{12}m_{21}\right) + B\left(m_{12}m_{11} - m_{12}m_{11}\right) &= -k_{0,x}m_{11} - \frac{1}{2}K_s k_{0,y}m_{12} \ , \\ \rightarrow A &= -k_{0,x}m_{11} - \frac{1}{2}K_s k_{0,y}m_{12} \ . \end{aligned} \tag{57}$$

Writing out the full form of A, and expressing this in terms of the real and imaginary parts of $\boldsymbol{k}_0$ (defined previously as $\boldsymbol{k}_0 = \hat{\boldsymbol{l}}_0 + \mathrm{i}\hat{\boldsymbol{m}}_0$), this is

$$-\begin{pmatrix} l_{0,x}\cos\phi_i + l_{0,y}\sin\phi_i \\ m_{0,x}\cos\phi_i + m_{0,y}\sin\phi_i \end{pmatrix} = \begin{pmatrix} l_{0,x} & \frac{1}{2}K_s l_{0,y} \\ m_{0,x} & \frac{1}{2}K_s m_{0,y} \end{pmatrix}\begin{pmatrix} m_{11} \\ m_{12} \end{pmatrix} \ . \tag{58}$$

Similarly, with $m_{22}\times$(Eq. (56)) $- m_{21}\times$(Eq. (55)),

$$\frac{1}{2}K_s\begin{pmatrix} l_{0,x}\sin\phi_i - l_{0,y}\cos\phi_i \\ m_{0,x}\sin\phi_i - m_{0,y}\cos\phi_i \end{pmatrix} = \begin{pmatrix} l_{0,x} & \frac{1}{2}K_s l_{0,y} \\ m_{0,x} & \frac{1}{2}K_s m_{0,y} \end{pmatrix}\begin{pmatrix} m_{21} \\ m_{22} \end{pmatrix} \ . \tag{59}$$

Solving Eqs. (58) and (59) gives the symplectic transfer matrix components that satisfy the horizontal spin matching conditions, granted that the matrix is also decoupled. Notably, infinitely many solutions will exist when the projections of $\hat{\boldsymbol{l}}_0$ and $\hat{\boldsymbol{m}}_0$ on the xy-plane lie along the same line (so the rows of the matrix are not linearly independent). This is *always* the case for the first and last solenoid modules, where the entering $\hat{\boldsymbol{n}}_0$ lies entirely in the xy-plane. In every other case, the universal solution is the only solution.

Only three quadrupoles are necessary for decoupling the solenoid module [12], and because the symplectic condition connects Eqs. (58) and (59), only three more quadrupoles are necessary for spin matching. However, when the entering/exiting $\hat{n}_0$ lies in the XY-plane (e.g. is vertical), the matrix in Eqs. (58) and (59) is degenerate. This leaves one variable free, and therefore only 5 quadrupoles are necessary for the outer-most (short) solenoid modules.

2.3.2 Longitudinal Spin Match

In the case of a coasting beam, to achieve a longitudinal spin match we would substitute a particle on the dispersive orbit $\boldsymbol{\zeta} = (\eta_x, \eta_{p_x}, \eta_y, \eta_{p_y}, 0, 1)^T$ into Eq. (41).

With RF, we would substitute the longitudinal eigenvector $\boldsymbol{v}_{III}$. The dispersion is easiest to substitute, and in the limit of $Q_s << Q_{x,y}$ it is a fine approximation. As with the horizontal spin matching conditions, integrals over the terms $(y'k_{0,x})'$ and $(x'k_{0,y})'$ are again zero; at the start and exit of the rotator there is no vertical dispersion and $\hat{\boldsymbol{n}}_0$ is vertical. Furthermore, terms proportional to y, y' in the bends will be zero because there is no vertical dispersion. This leaves

$$\int_{s_{in}}^{s_{out}} \boldsymbol{\omega} \cdot \boldsymbol{k}\, ds = \int_{8\text{ sols}} K_s(1+a)\left\{a\gamma_0\left[\left(\eta_{p_x} + \frac{1}{2}K_s\eta_y\right)k_{0,x} + \left(\eta_{p_y} - \frac{1}{2}K_s\eta_x\right)k_{0,y}\right] + k_{0,s}\right\} ds - \int_{4\text{ bends}} g_x\left(a\gamma_0 - \frac{a}{\gamma_0}\right)k_{0,y}\, ds\,. \tag{60}$$

Assuming $(1+a) \approx 1$ so that $(x'k_{0,x} + y'k_{0,y})$ is constant within a solenoid, the terms proportional to $a\gamma_0$ in the integral over the solenoids gives the exact same conditions as the horizontal spin matching conditions. This is because there is zero vertical dispersion and zero coupling entering and exiting the solenoid module, and the horizontal dispersion will propagate over the solenoid module according to the same 2×2 horizontal transfer matrix. Defining $\phi_i = 2(K_sL)_i(1+a) \approx 2(K_sL)_i$ as the spin precession in the i-th solenoid module, $\psi_j = a\gamma_0(g_xL)_j$ the spin precession in the j-th bend module, and finally assuming $a/\gamma_0 \approx 0$, the longitudinal spin matching conditions are

$$a\gamma_0 \sum_{i=1}^{4} H_i + \sum_{i=1}^{4} k_{0s,i}\phi_i - \sum_{j=1}^{4} k_{0y,j}\psi_j = 0\,. \tag{61}$$

Therefore, a longitudinal spin match can be achieved by choosing the geometry (spin rotation angles in the bends) and solenoids strengths (spin rotation angles in the solenoids), and having a horizontal spin-match.

2.4 Spin Rotator Configurations

At the time of this dissertation writing, the spin rotator configuration (solenoid strengths and bend angles) is "finalized", for those values shown in Table 1. A longitudinal strong synchrobeta spin match is *not* satisfied at 18 GeV, however the polarization has been rescued by a novel method developed in this dissertation called *Best Adjustment Groups for ELectron Spin (BAGELS)*. BAGELS also enables simultaneous polarization, orbit, and optics control in electron storage rings, providing an effective method to correct polarization in operation, preserve high polarization while correcting the optics, and preserve high polarization while generating vertical emittance (necessary for beam-size matching with the hadron beam at the IP). BAGELS, which has become an essential and necessary part of the EIC-ESR design, is discussed and presented in detail in Sec.4. Nonetheless, much work was done leading to the development of BAGELS. To set the stage for the next several chapters, in this section we describe various choices for the solenoid strengths and bend angles, and their

implications on the design. The SymPy symbolic computer algebra system was used extensively for the derivations in this section [15].

Following Fig. 2, for a vertical incoming $\hat{\boldsymbol{n}}_0$ we require some $\psi_{1,2,3,4}$ and $\phi_{1,2,3,4}$ to rotate $\hat{\boldsymbol{n}}_0$ to the longitudinal at the IP, then rotate back to vertical. A configuration symmetric about the IP, such that $\psi_1 = \psi_4$, $\psi_2 = \psi_3$, $\phi_1 = \phi_4$, and $\phi_2 = \phi_3$, is also sought; it can be shown that if $\hat{\boldsymbol{n}}_0$ is rotated from vertical to $\pm\hat{\boldsymbol{z}}$, then a symmetric arrangement will rotate it back to vertical. Now, we consider the solenoid spin precession angles ϕ_1 and ϕ_2 that we would need to rotate $\hat{\boldsymbol{n}}_0$ from vertical in the arc to longitudinal at the IP, given the bend precession angles ψ_1 and ψ_2. Letting $\mathsf{R}_x(\alpha)$, $\mathsf{R}_y(\alpha)$, and $\mathsf{R}_z(\alpha)$ correspond to the SO(3) rotation matrices around the x, y, and z axes respectively by an angle α, from arc-to-IP we have

$$\begin{pmatrix} 0 \\ 0 \\ \sigma \end{pmatrix} = \mathsf{R}_y(\psi_2)\mathsf{R}_z(\phi_2)\mathsf{R}_y(\psi_1)\mathsf{R}_z(\phi_1)\begin{pmatrix} 0 \\ 1 \\ 0 \end{pmatrix}, \tag{62}$$

where $\sigma = \pm 1$. After multiplying the rotations, this gives three equations constraining the angles. The first two equations, however, can be expressed as a linear homogeneous system in $\cos\phi_1$ and $\sin\phi_2$. Therefore, because we cannot simultaneously have $\cos\phi_1 = \sin\phi_2 = 0$the determinant of this system must be zero. This determinant equation, along with the third equation in the overall system, gives the general conditions

$$\sin(\psi_1)\sin(\psi_2)\cos(\phi_2) - \cos(\psi_1)\cos(\psi_2) = 0\,, \tag{63a}$$

$$\left[\sin(\psi_1)\cos(\psi_2) + \sin(\psi_2)\cos(\psi_1)\cos(\phi_2)\right]\sin(\phi_1) + \sin(\psi_2)\sin(\phi_2)\cos(\phi_1) = \sigma\,. \tag{63b}$$

The solutions to these conditions have several cases which we must consider carefully. For $n, m, k \in \mathbb{Z}$,

1. If $\psi_1 = n\pi$ then we must have $\psi_2 = m\pi - \frac{\pi}{2}$ to satisfy Eq. (63a). Substituting this into Eq. (63b) gives

$$\sin(\phi_2)\cos(\phi_1) + (-1)^n\cos(\phi_2)\sin(\phi_1) = (-1)^{m+1}\sigma\,, \tag{64}$$

   which simplifies to

$$\sin(\phi_2 + (-1)^n\phi_1) = (-1)^{m+1}\sigma\,. \tag{65}$$

   Therefore,

$$\phi_2 + (-1)^n\phi_1 = \frac{\pi}{2}(-1)^{m+1}\sigma + 2k\pi\,. \tag{66}$$

2. If $\psi_2 = n\pi$ then we must have $\psi_1 = m\pi - \frac{\pi}{2}$ to satisfy Eq. (63a). Substituting this in Eq. (63b) gives

$$\sin(\phi_1) = (-1)^{n+m+1}\sigma\,. \tag{67}$$

Therefore,

$$\phi_1 = \frac{\pi}{2}(-1)^{n+m+1}\sigma + 2k\pi \ , \ \phi_2 \text{ free} \ . \tag{68}$$

In this case ϕ_2 is free, because $\hat{\boldsymbol{n}}_0$ will be pointing along the $\pm\hat{\boldsymbol{z}}$ direction when it reaches that solenoid module after being rotated by ϕ_1.

3. If $\psi_1 \neq n\pi$ and $\psi_2 \neq m\pi$, then we can solve Eq. (63a) directly. With some algebra, we obtain the solution

$$\phi_1 = \text{atan2}\left[\sigma\frac{\cos(\psi_2)}{\sin(\psi_1)},\ s\sigma\sin(\psi_2)\sqrt{1-\cot^2(\psi_1)\cot^2(\psi_2)}\right], \tag{69a}$$

$$\phi_2 = \text{atan2}\left[s\sqrt{1-\cot^2(\psi_1)\cot^2(\psi_2)},\ \cot(\psi_1)\cot(\psi_2)\right], \tag{69b}$$

where $s = \pm 1$. In order to have a solution, $-1 < \cot(\psi_1)\cot(\psi_2) < 1$.

We now consider which angles would provide a longitudinal strong synchro-beta spin match. Per Eq. (61), if a horizontal spin match is satisfied then for a longitudinal spin match we have

$$\sum_{i=1}^{4} k_{0s,i}\phi_i - \sum_{j=1}^{4} k_{0y,j}\psi_j = 0 \ . \tag{70}$$

This sum can be evaluated for arbitrary choice of angles, and those angles which make the real and imaginary parts equal to zero yield a longitudinal spin match. We now consider this sum for the three cases of solutions (let $n, m, k \in \mathbb{Z}$):

1. For $\psi_1 = n\pi$, $\psi_2 = m\pi - \frac{\pi}{2}$, and $\phi_2 + (-1)^n\phi_1 = \frac{\pi}{2}(-1)^{m+1}\sigma + 2k\pi$, the real part of the sum simplifies to $0 = 0$ and the imaginary part simplifies to the requirement

$$\sin(\phi_1) = \sigma\frac{(-1)^{m+n}(2m-1)}{2n} \ , \ n \neq 0 \ . \tag{71}$$

Therefore solutions only exist when

$$|2m-1| \leq |2n| \ . \tag{72}$$

2. For $\psi_2 = n\pi$, $\psi_1 = m\pi - \frac{\pi}{2}$, and $\phi_1 = \frac{\pi}{2}(-1)^{n+m+1}\sigma + 2k\pi$, ϕ_2 free, the real and imaginary parts both simplify to the same condition,

$$(-1)^{n+1}\cos(\phi_2) + \frac{1}{2m-1}\sin(\phi_2) = (-1)^n\frac{2n}{2m-1} \ . \tag{73}$$

Using the harmonic addition theorem, we can rewrite the LHS of this equation as a single sinusoid. After some simplification,

$$\cos\left[\phi_2 + (-1)^n\,\text{atan2}(1,\ 2m-1)\right] = -\frac{2n}{\sqrt{1+(2m-1)^2}} \ . \tag{74}$$

Therefore solutions only exist when

$$|2n| \leq \sqrt{1 + (2m-1)^2}\,. \tag{75}$$

3. For $\psi_1 \neq n\pi$, $\psi_2 \neq m\pi$, and ϕ_1, ϕ_2 satisfy Eqs. (69), a simple algebraic expression giving the longitudinal spin matching conditions is not obtainable – numerical solution is required.

Finally, it is insightful to consider the spin phase advance of $\boldsymbol{k}_0$ over the rotator, which we will refer to as α_s, given some choice of spin rotation angles. This is most easily obtained from the spin transport quaternion over the entire rotator, which will be some rotation around the vertical axis; this angle is α_s. In general, this gives

$$\sin(2\pi\alpha_s/2) = \sin(\psi_1)\cos(\psi_2)\cos(\phi_2) + \cos(\psi_1)\sin(\psi_2)\,. \tag{76}$$

Therefore, for each class of solution,

1. For $\psi_1 = n\pi$, $\psi_2 = m\pi - \frac{\pi}{2}$, and $\phi_2 + (-1)^n\phi_1 = \frac{\pi}{2}(-1)^{m+1}\sigma + 2k\pi$, we obtain $\alpha_s = \frac{1}{2}(-1)^{m+n+1}$.

2. For $\psi_2 = n\pi$, $\psi_1 = m\pi - \frac{\pi}{2}$, and $\phi_1 = \frac{\pi}{2}(-1)^{n+m+1}\sigma + 2k\pi$, ϕ_2 free, we obtain $\alpha_s = \frac{(-1)^{n+m+1}}{\pi}\arcsin[\cos(\phi_2)]$.

3. For $\psi_1 \neq n\pi$, $\psi_2 \neq m\pi$, and ϕ_1, ϕ_2 satisfy Eqs. (69), we obtain the simple form $\alpha_s = \frac{1}{\pi}\arcsin[\cos(\psi_1)/\sin(\psi_2)]$.

We remark that case 1 is "special", because it is impossible to distinguish a rotation of $+\pi$ from a rotation of $-\pi$, and therefore the values of m and n really do not matter. Furthermore, in this case if the solenoids were turned off, α_s would be $\frac{2(n\pi+m\pi-\pi/2)}{2\pi} = n + m - \frac{1}{2}$. Because only the fractional part of the spin tune has any meaning and n, m are integers, α_s over the rotator is still just π. Therefore, for case 1 the closed orbit spin tune is unchanged if the solenoids are turned on vs. off.

Each solution case, its requirement for a longitudinal spin match, and α_s is summarized in Table 2.

Table 2: With Fig. 2, the various solutions for ϕ_1 and ϕ_2 to rotate $\hat{\boldsymbol{n}}_0$ to $\sigma\hat{\boldsymbol{z}}$, $\sigma = \pm 1$, from $\hat{\boldsymbol{y}}$ given some ψ_1, ψ_2 and assuming a symmetric layout such that $\phi_1 = \phi_4$, $\phi_2 = \phi_3$, $\psi_1 = \psi_4$, and $\psi_2 = \psi_3$. Here $n, m, k \in \mathbb{Z}$, LSM stands for longitudinal spin match, and α_s corresponds to the spin phase advance of $\boldsymbol{k}_0$ across the rotator.

	Case 1	**Case 2**	**Case 3**
Bends	$\psi_{1,4} = n\pi \rightarrow \psi_{2,3} = m\pi - \dfrac{\pi}{2}$	$\psi_{2,3} = n\pi \rightarrow \psi_{1,4} = m\pi - \dfrac{\pi}{2}$	$\psi_1 \neq n\pi, \psi_2 \neq m\pi$
Solenoids	$\phi_2 + (-1)^n \phi_1 = \dfrac{\pi}{2}(-1)^{m+1}\sigma + 2k\pi$	$\phi_1 = \dfrac{\pi}{2}(-1)^{n+m+1}\sigma + 2k\pi\ ,\ \phi_2$ free	$c_2 = \cot(\psi_1)\cot(\psi_2)$ $\phi_1 = \operatorname{atan2}\left[\sigma\dfrac{\cos(\psi_2)}{\sin(\psi_1)},\ s\sigma\sin(\psi_2)\sqrt{1-c_2^2}\right],$ $\phi_2 = \operatorname{atan2}\left[s\sqrt{1-c_2^2},\ c_2\right],$
LSM Condition	$\phi_1 = \sigma(-1)^{m+n}\arcsin\left[\dfrac{2m-1}{2n}\right]$	$\phi_2 = \arccos\left[-\dfrac{2n}{\sqrt{1+(2m-1)^2}}\right]$ $+ (-1)^{n+1}\operatorname{atan2}(1,\ 2m-1)$	Numerical solution required
α_s **[2π]**	$\dfrac{(-1)^{m+n+1}}{2}$	$\dfrac{(-1)^{n+m+1}}{\pi}\arcsin\left[\cos(\phi_2)\right]$	$\dfrac{1}{\pi}\arcsin\left[\dfrac{\cos(\psi_1)}{\sin(\psi_2)}\right]$

2.5 Lattice Versions

Per Eq. (19), we have $\psi_1 = -\theta_1 a\gamma_0$ where θ_1 is the *orbit* precession in the first bend module; the spin precession in bend modules is directly connected to the geometry of the ring. Therefore, since we don't want to change the geometry of the ESR for the various energy cases, it is insightful to consider the solutions presented in Table 2 given some choice of ψ_1 and ψ_2. Figure 7 shows, for a given ψ_1 and ψ_2 the regions where ϕ_1 and ϕ_2 can (green) and cannot (red) be set to achieve longitudinal spin at the IP, as well as a black line corresponding to when a longitudinal spin match (LSM) is possible. The corners of each tile correspond to either case 1 or 2, and the bodies of each tile correspond to case 3. In this plot, a given geometry will correspond to a straight line that goes through the origin with slope $\psi_2/\psi_1 = \theta_2/\theta_1$. Then, once the energy is defined at one point along this line, the energies at all different points are defined; as γ_0 is changed, the position along the line changes linearly.

Early versions of the 18 GeV EIC-ESR, specifically those $\leq$ v5.6, had the first class of solutions with $\psi_1 = -\pi$ and $\psi_2 = -\pi/2$. This corresponds to the right-most "x" of the yellow line in Fig. 7. In this case, the closed orbit spin tune is unchanged if the rotator is on vs. off, and so we can select the exact energy for a half-integer spin tune using the formula for a perfectly flat, aligned ring with only dipoles and regular quadrupoles, $\nu_0 = a\gamma_0$. The 18 GeV case was therefore selected to have $a\gamma_0 = 40.5$, which corresponds to the exact energy $E = 17.846$ GeV.

The 18 GeV v5.3 specifically had a longitudinal spin match, and therefore per Eqs. (66) and (71) required the specific solenoid module spin rotation angles $\phi_1 = (-30°)\sigma$ and $\phi_2 = (-120°)\sigma$. Using Eq. (19), for the long solenoid module this corresponds to the integrated field

$$|B_s L| = \frac{p_0}{q} \frac{120 \frac{\pi}{180}}{1+a} = 124.53 \text{ T m} . \tag{77}$$

This is massive. In the v5.3, each of the two solenoids in the long solenoid module was 9 m long, corresponding to 6.9 T field strengths. In the v5.6, the solenoids in the long module were only 5.5 m long, which would correspond to 11.3 T field strengths to achieve a longitudinal spin match. This is impractical, and ultimately led to the dropping of the LSM. Instead for v5.6, per case 1 in Table 2, the solution $\phi_1 = 0$, $\phi_2 = -\frac{\pi}{2}$ was selected so that only the long solenoid module is "on" at 18 GeV. This corresponds to a slightly more reasonable 8.5 T for the long solenoids in v5.6, at the cost of a LSM. However, now that we have chosen an energy for a point on the plot of Fig. 7, the energies at all other points are also defined. In this case, the lowest energy case we can achieve in the v5.6 (the left-most "x" of the yellow line in Fig. 7) is 5.95 GeV; this is a quite a lot higher than the 5 GeV requested by the high energy physics experimentalists.

If we would like to support a low-energy closer to 5 GeV, then we can do two things. Firstly, we could keep the ratio θ_2/θ_1 constant, but add some angle to both θ_1 and θ_2 so that the lowest possible energy case is closer to 5 GeV – this would make the 18 GeV case "move up" along the yellow line. The problem

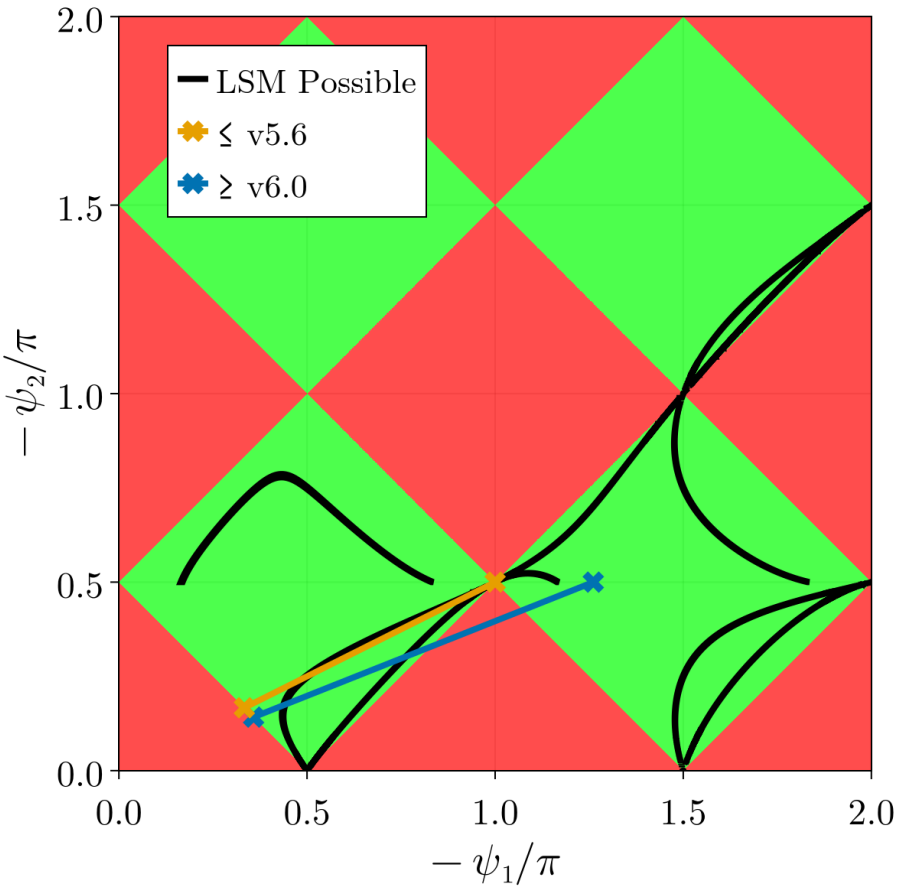

Figure 7: Regions where longitudinal spin at the IP is achievable (green) and not achievable (red) for the spin rotator in Fig. 2, given some bend module spin precession angles ψ_1 and ψ_2. The black lines specify where a longitudinal spin match (LSM) is possible, and straight lines going through the origin correspond to constant bend geometries.

with this, however, is that for $\psi_2 > \pi/2$, the long solenoid precession angle solution ϕ_2 essentially "continues" from the 120° at the corner of the tile, not 90°; the new solution is not near $\phi_2 = -\pi/2$ but near $\phi_2 = -120°$. The integrated field strength would then still be too large.

Alternatively, we could keep θ_2 constant so that the more manageable $\phi_2 = -\pi/2$ remains the solution for 18 GeV, and increase θ_1 until the lower bound of the new line with slope θ_2/θ_1 allows for 5 GeV. This was ultimately the solution decided for the v6.0 lattice, and remains the current bend configuration at the

time of this dissertation writing. One thing to note per Fig.7 is that the lower bound is defined by the curve $\psi_2 = \frac{\pi}{2} - \psi_1$, and so therefore at the lower bound $\cos(\psi_1) = \sin(\psi_2)$. From Table 2, this corresponds to a $\alpha_s = \frac{1}{2}$; the closed orbit spin tune is unchanged if the rotator is on vs. off for the low energy bound. Therefore, the amount of θ_1 added corresponded to making $a\gamma_0 = 11.5$ ($E = 5.07$ GeV) at the right at the lower bound. Furthermore, by keeping the 18 GeV case at $\psi_2 = -\pi/2$ and having $\phi_1 = 0$, it can be shown that α_s is also unchanged whether or not the rotator is on. Therefore the 18 GeV case is kepy at $a\gamma_0 = 40.5$. The "finalized" geometry for v6.0+ is defined by the blue line in Fig. 7, with the left-most "x" corresponding to $E = 5.07$ GeV and the right-most "x" corresponding to $E = 17.846$ GeV.

The solenoid and bend module spin precession angles for the various 18 GeV ESR versions are summarized in Table 3.

Table 3: Solenoid ($\hat{s}$) and bend ($\hat{y}$) module spin precession angles for various 18 GeV ESR lattices, using the right-handed basis ($\hat{x}, \hat{y}, \hat{s}$) with $\hat{s}$ pointing along the longitudinal in Fig. 2

	Solenoids		**Bends**	
	$\phi_{1,4}$	$\phi_{2,3}$	$\psi_{1,4}$	$\psi_{2,3}$
ESR v5.3 (LSM)	$-30°$	$-120°$	$-180°$	$-90°$
ESR v5.6 (No LSM)	$0°$	$-90°$	N/A	$-90°$
ESR v6.0 (No LSM)	$0°$	$-90°$	N/A	$-90°$

3 Partial Longitudinal Spin Match Attempt

3.1 Background

As shown in Fig. 6, the lack of a longitudinal spin match has severe consequences on the polarization for the 18 GeV case of the EIC-ESR. Furthermore, the eventual insertion of a vertical emittance creator in the ESR – necessary to match the electron and ion beam sizes – will have detrimental effects on polarization unless carefully implemented. Misalignments will also degrade the polarization further. Without some kind of further polarization correction, achieving the minimum polarization requirement poses a significant, if not fatal, problem.

The longitudinal spin match was originally dropped going from v5.3 to v5.6 primarily due to various undesirable nonlinear effects, including low polarization [22], that resolved when turning off the short solenoid module (thus losing the LSM) and setting the dispersion to zero in the long solenoid module. These effects were later determined to be caused by a 2^{nd} order synchrobeta resonance excited by vertical dispersion in quadrupoles - as is the case when entering a solenoid module with nonzero horizontal dispersion. By changing

the tunes, the effects may be resolved; the nonlinear polarization can have excellent agreement with the analytical calculation [24]. While this finding led to a change in the working point, it also re-opened the question of whether or not a LSM should be achieved in the ESR. Unfortunately, as described in Sec. 2.5, the integrated field strengths in the solenoids required for a longitudinal spin match are simply too large to feasibly engineer. Therefore, another solution must be found.

One idea to remedy this problem is to use turn on the solenoids in the second interaction region in some way such that a partial LSM is achieved, as shown in Fig. 8. In this chapter, an in-depth study is performed analyzing the feasibility and efficacy of such an approach.

3.2 Partial LSM and Results

While a full LSM over a single IR is not feasible, it may be possible to achieve a partial LSM around the ring; for the 1-IP case, using the solenoids in the 2$^{\text{nd}}$ IR we can attempt to spin match from the start of the 6 o'clock IR to the end of the last active solenoid in the 8 o'clock IR. The spin matching condition for this case looks the same as that in Eq. (61), but the solenoid sums are now over 8 solenoid modules and the bend sum is over 9 bend modules (including the bend between IR-6 and IR-8, ψ_5). Thus, with horizontal spin matching $H_i = 0$ for each i, and assuming a constant geometry (constant ψ_i's), the goal is to minimize g in Eq. (78) where ϕ_5, ϕ_8 are the IR-8 short solenoid module precession angles and ϕ_6, ϕ_7 the long solenoid module precession angles.

$$g(\phi_5, \phi_6, \phi_7, \phi_8) = \sum_{i=1}^{8\text{ sol}} \phi_i k_{0s,i} - \sum_{j=1}^{9\text{ bend}} \psi_j k_{0y,j} \,. \tag{78}$$

Each ϕ_i must be chosen so that $\hat{n}_0$ returns to vertical. For the v6.0, due to the bend module precession angles, in the symmetric case this leaves only $\phi_{5,8} = 0$ and $\phi_6 = \phi_7$. For the v5.6, there are three simple symmetric cases: 1) $\phi_5 = \phi_8$ and $\phi_6 = \phi_7$; 2) $\phi_5 = \phi_6$ and $\phi_7 = \phi_8$; 3) $\phi_5 = -\phi_7$ and $\phi_6 = -\phi_8$. We start with the v5.6. For each of the three cases, surfaces of $|g|$ like Fig. 9 may be generated. With

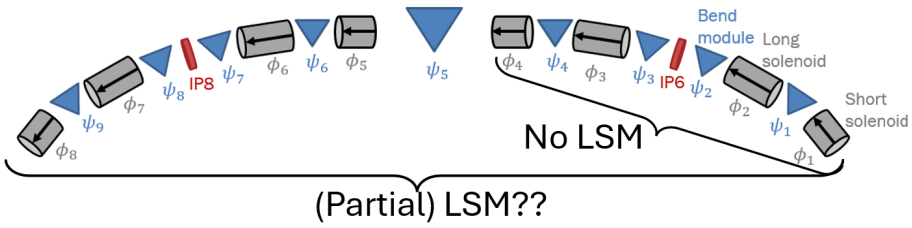

Figure 8: Schematic displaying the idea of a partial longitudinal spin match (LSM) using the second spin rotator.

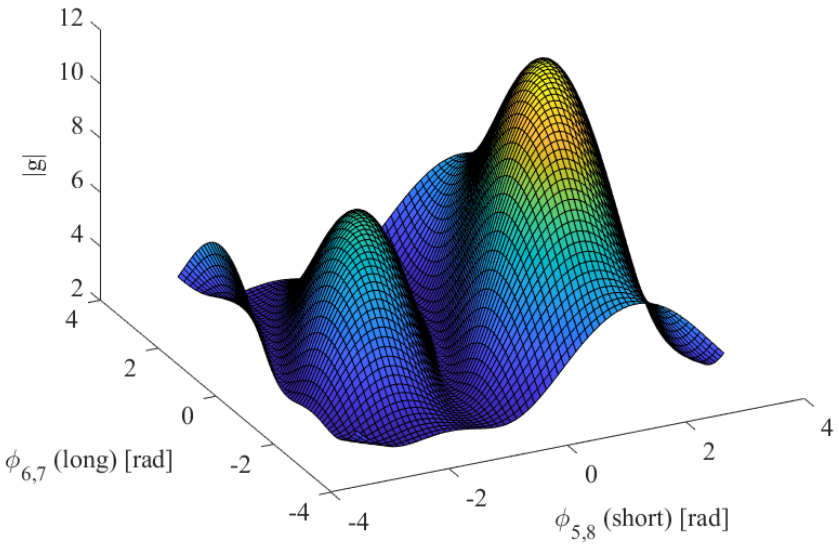

Figure 9: $|g(\phi_5, \phi_6)|$ with $\phi_5 = \phi_8$ and $\phi_6 = \phi_7$ (case 1) for the ESR v5.6.

the IR-8 solenoids all off, $|g| = \pi$. Because the choice of angles for minimum $|g|$ is not unique, the angles which minimize the length of the section we attempt to partially LSM are selected as optimal.

The same minimum value $|g_{\min}| = 2.2561$ was obtained for each case, and is dependent on the spin precession angle in the bend between IR-6 and IR-8 (ψ_5). In fact, if $\psi_5 = n\pi$, $n \in \mathbb{Z}$, then $g_{\min} = 0$ and thus a full LSM using the 2$^{\text{nd}}$ IR is achievable. Unfortunately, this is not the case, and such geometry changes to make $\psi_5 = n\pi$ are not feasible. We determined the best scheme to be one of case 2 with $\phi_{7,8} = 0$, so that only the first set of solenoids before IP-8 are on; this achieves a partial LSM at the earliest point in the lattice. The scheme was implemented into a Bmad lattice and both optics matched and horizontally spin matched using Tao. The resulting increase in T was 0.4 min, as shown in Table 4. For the v6.0, which has only one valid solenoid setting ($\phi_{5,8} = 0$ and $\phi_6 = \phi_7$), $|g_{\min}| = 2.2564$. Thus, we expect the result to be similar to that for the v5.6.

For the 2-IP v5.6, where both IR-6 and IR-8 have the same solenoid settings, $|g| = 5.7858$. By flipping the polarity of the IR-8 solenoids (and thus the sign of the polarization at IP-8), $|g| = 2.45$. This simple change significantly improves T, as shown in Table 4. A similar result is seen in the v6.0.

Table 4: Replacement Times for 18 GeV ESR Lattices

18 GeV ESR Lattices	T_+ **[min]**	T_- **[min]**	T **[min]**
v5.3 1-IP, LSM	77.8	6.9	12.6
v5.3 2-IP, LSM	29.2	6.4	10.6
v5.6 1-IP, no LSM	11.0	4.1	6.0
v5.6 1-IP, partial LSM	11.5	4.4	6.4
v5.6 2-IP, no LSM	4.0	2.5	3.1
v5.6 2-IP, flip IR-8 polarity	7.8	3.9	5.2
v6.0 1-IP, no LSM	9.8	3.8	5.5
v6.0 2-IP, no LSM	4.7	2.8	3.5
v6.0 2-IP, flip IR-8 polarity	7.5	4.0	5.2

4 BAGELS Theory

4.1 Initial Approach

As evident by the spin-orbit integral in Eq. (26), to achieve a spin match one must set $\boldsymbol{\omega}$ and/or $\boldsymbol{k}_0$ so the spin-orbit coupling cancels. Per Eq. (23), $\boldsymbol{k}_0$ corresponds to $\hat{\boldsymbol{n}}_0$ and the spin tune evolution around the ring (zeroth order spin precession on the closed orbit), while $\boldsymbol{\omega}$ corresponds to the first-order magnetic fields around the closed orbit (the optics) given the $\boldsymbol{k}_0$. Changes to $\boldsymbol{k}_0$ are usually viewed as challenging, as they are connected with the geometry of the ring (spin precession in the bends) and solenoid strengths. In the ESR, analytical conditions were derived using Eq. (26) to achieve both a horizontal and longitudinal spin match outside the spin rotator [16, 21]. The horizontal spin match is achieved by choosing the optics in each solenoid module (setting $\boldsymbol{\omega}$), while the longitudinal spin match is achieved by both having a horizontal spin match and choosing special solenoid strengths (setting $\boldsymbol{k}_0$). However, the solenoid strength necessary for such is 11 Tesla, which is obviously infeasible. The lack of a longitudinal spin match excites a significant $\boldsymbol{d}$ around the ring.

Without any other systematic method to change $\boldsymbol{k}_0$, the only way to achieve some longitudinal spin match is to "steal" from part of the horizontal spin match by changing $\boldsymbol{\omega}$. Thus, we seek a method that minimizes the leftover $\boldsymbol{d}$ by intentionally tilting $\hat{\boldsymbol{n}}_0$ near and through the rotator using vertical orbit bumps. The corresponding changes to $\boldsymbol{k}_0$ should accumulate spin-orbit coupling which perfectly cancels that leftover by the rotator. The orbit bumps therefore should be placed in the periodic FODO arcs directly around the spin rotator, and basically have a net effect of "walking down" the spin orbit coupling function to zero on either side of the rotator. Furthermore, the bumps must have essentially no impact on the optics around the ring.

An arbitrary choice of vertical orbit bump in the periodic arc section will create both delocalized vertical dispersion and delocalized transverse coupling (caused by the skew quadrupole feed-down term from a nonzero vertical closed

orbit through the sextupoles). Both of these effects must, at least to first-order in the phase space coordinates, cancel by design of the bump. First, let us consider the coupling caused by the nonzero vertical orbits through the sextupoles. Because the chromatic beta-beat oscillates with $2\times$ the betatron oscillation frequency, chromatic sextupoles that are separated by 90° in betatron phase will work against each other. Therefore, to coherently cancel the chromatic beta-beat, the sextupoles in a periodic arc are usually split into either two (for a 90° betatron phase advance per cell) or three (for a 60° betatron phase advance per cell) families per transverse plane, with each sextupole in a family separated by 180° in betatron phase. We can take advantage of the chromatic sextupoles' regular placement to construct a bump that automatically cancels its own generated coupling. Consider the case of a 90° phase advance per cell, as in the arcs of the 18 GeV EIC-ESR. If we turn on a π bump, the orbit will go through all four different strength sextupoles (two families per plane) once with a positive vertical offset. Therefore, in order to cancel this generated coupling, we need to use another π bump of opposite strength such that the orbit goes through the four sextupoles again with the same magnitude but opposite sign. Therefore, we can place the second opposite π bump anywhere $\pi n,\ n \in \mathbb{Z}$, in betatron phase away from the first bump in order to cancel the coupling. However, if we would also like to cancel the vertical dispersion wave generated by the first, then the first corrector coil of the second π bump must be $(2n+1)\pi$ away from the last corrector coil of the first π bump. This type of vertical orbit bump, which we henceforth refer to as an "opposite π pair" shown in Fig. 10, has minimal impacts on the optics, creating no delocalized transverse coupling nor delocalized vertical dispersion. With bending magnets between the corrector coils, a delocalized tilt to $\hat{\boldsymbol{n}}_0$ is produced. This makes the opposite π pair ideal for spin matching by intentionally changing $\boldsymbol{k}_0$.

If the orbit excursions in the sextupoles are kept small, we can overlap all different opposite π pairs in an arc and still have the orbit close and generate no delocalized vertical dispersion nor delocalized coupling. As such, we can construct special vertical orbit bumps, each composed of a linear combination of many opposite π pairs, to minimize $\boldsymbol{d}$ in the bends where its contribution to radiative depolarization is most significant. Henceforth, we will refer to any choice of vertical orbit bump type that makes up a composite vertical orbit bump as a *basis bump*. In this case, for spin matching, the basis bump choice is the opposite π pair.

If all bends in the ring have nearly the same length and strength, then considering only $\boldsymbol{d}$ at all bends is sufficient to capture the effects of radiative depolarization. More generally, per Eq. (4), $\boldsymbol{d}\sqrt{L|\boldsymbol{g}|^3}$ at the ends of all bends could be considered, where $\boldsymbol{g}$ and L are respectively the bend curvature and length. For the following formulation, we will assume all the bends have the same strengths and lengths for notational simplicity. Parametrizing the strength of each selected basis bump as θ_i, the values of $\boldsymbol{d}$ at r selected bends can be written as a function of c selected basis bumps, to first-order in the strengths $\boldsymbol{\theta} = (\theta_1, ..., \theta_c)^T$, as

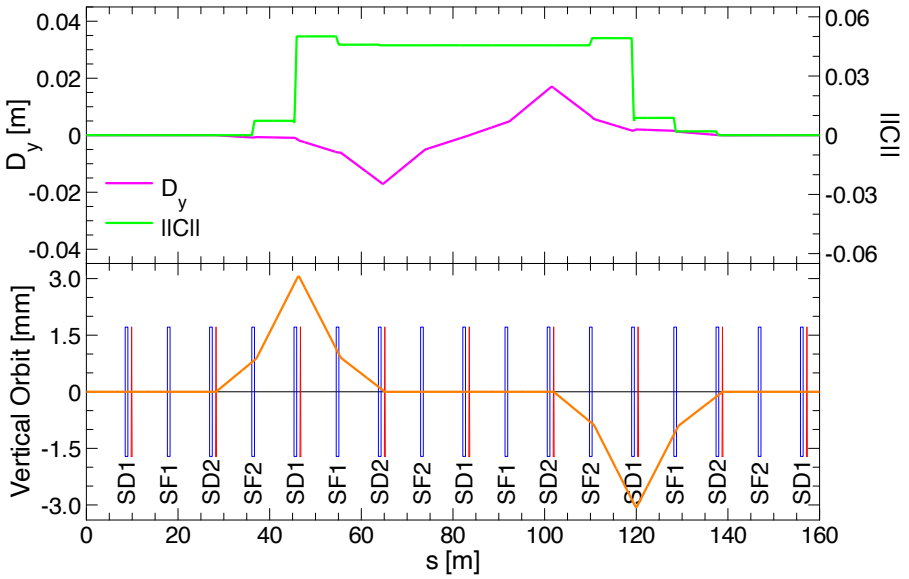

Figure 10: Opposite π pair placed in a periodic FODO beamline with 90° phase advance per cell and two sextupole families per plane (SF for the horizontal, SD for the vertical). Sextupoles are specified as blue rectangles, vertical corrector coils as red triangles, and the quadrupoles and bends are not shown. The bump's corresponding vertical dispersion D_y and normalized coupling matrix norm $\|\bar{C}\|$ are plotted above [18]. The opposite π pair creates only localized coupling and localized vertical dispersion, but a delocalized tilt to $\hat{\boldsymbol{n}}_0$ due to the bending magnets between the corrector coils, making it ideal for spin matching.

$$\boldsymbol{f_d} \approx (\boldsymbol{f_d})_0 + \mathsf{R}_{\boldsymbol{d}}\boldsymbol{\theta}\,, \tag{79}$$

$$\boldsymbol{f_d} = \begin{pmatrix} \boldsymbol{d}_1 \\ \vdots \\ \boldsymbol{d}_r \end{pmatrix},\ \mathsf{R}_{\boldsymbol{d}} = \begin{pmatrix} \frac{\partial \boldsymbol{d}_1}{\partial \theta_1} & \cdots & \frac{\partial \boldsymbol{d}_1}{\partial \theta_c} \\ \vdots & \ddots & \vdots \\ \frac{\partial \boldsymbol{d}_r}{\partial \theta_1} & \cdots & \frac{\partial \boldsymbol{d}_r}{\partial \theta_c} \end{pmatrix}_{\mathbf{0}}\,, \tag{80}$$

where $\mathsf{R}_{\boldsymbol{d}}$ is the response matrix of $\boldsymbol{d}$ for each basis bump. Any arbitrary $\boldsymbol{\theta}$ defines a composite vertical closed orbit bump - a linear combination of the basis bumps - that can be scaled up and down using a knob in the control room of the real accelerator. We seek a $\boldsymbol{\theta}$ that sets the LHS of Eq. (79) closest to zero.

Almost always, $3r > c$, and for this overdetermined system we can use any modern linear algebra software package to calculate a least-squares solution that minimizes $\|\mathsf{R}_{\boldsymbol{d}}\boldsymbol{\theta} + (\boldsymbol{f_d})_0\|^2$. However, the problem with this approach is that the least-squares solution will have too large strengths for the basis bumps that have little impacts on $\boldsymbol{d}$ in the bends, exceeding the linear response regime and creating large orbit excursions. Naively, one could just iteratively exclude basis bumps that have the smallest columns in $\mathsf{R}_{\boldsymbol{d}}$. However, this approach is not general, as it is entirely possible, and in fact likely, that basis bumps that have large impacts alone may have little impact when paired together in a linear combination, and vice-versa. We thus require a systematic way to reduce our space to a minimal number k of special $\boldsymbol{\theta}$'s that maximally scale when multiplied by $\mathsf{R}_{\boldsymbol{d}}$. Specifically, we seek

$$\underset{\boldsymbol{\theta}_1,...,\boldsymbol{\theta}_k}{\text{argmax}} \frac{\|\mathsf{R}_{\boldsymbol{d}}\boldsymbol{\theta}\|^2}{\|\boldsymbol{\theta}\|^2} = \underset{\boldsymbol{\theta}_1,...,\boldsymbol{\theta}_k}{\text{argmax}} \frac{\boldsymbol{\theta}^T\mathsf{A}\boldsymbol{\theta}}{\boldsymbol{\theta}^T\boldsymbol{\theta}} \ , \tag{81}$$

where $\mathsf{A} = \mathsf{R}_{\boldsymbol{d}}^T\mathsf{R}_{\boldsymbol{d}}$ and $\boldsymbol{\theta}_1, ..., \boldsymbol{\theta}_k$ are all orthogonal to each other. These correspond to composite vertical orbit bumps which we can use to maximally, and orthogonally, impact the spin-orbit coupling function in the bends. Readers may recognize this well-known dimensionality reduction technique as principal component analysis (PCA). The quotient in Eq. (81) is called the *Rayleigh quotient* of A and $\boldsymbol{\theta}$, and we seek its maximizers. We follow the approach in [10]. It is obvious that we can express this problem equivalently as maximizing $\boldsymbol{\theta}^T\mathsf{A}\boldsymbol{\theta}$ subject to the constraint $\boldsymbol{\theta}^T\boldsymbol{\theta} = 1$. Using the method of Lagrangian multipliers, the Lagrangian is

$$\mathcal{L} = \boldsymbol{\theta}^T\mathsf{A}\boldsymbol{\theta} + \lambda\left(\boldsymbol{\theta}^T\boldsymbol{\theta} - 1\right) \ . \tag{82}$$

The stationary points of the Lagrangian are calculated as the solutions to

$$\frac{\partial\mathcal{L}}{\partial\boldsymbol{\theta}} = 2\mathsf{A}\boldsymbol{\theta} - 2\lambda\boldsymbol{\theta} = 0 \ \rightarrow \ \mathsf{A}\boldsymbol{\theta} = \lambda\boldsymbol{\theta} \ , \tag{83}$$

where we use the fact that, because the covariance matrix A is symmetric, $\partial_{\boldsymbol{\theta}}(\boldsymbol{\theta}^T\mathsf{A}\boldsymbol{\theta}) = 2\mathsf{A}\boldsymbol{\theta}$. Also, because $\boldsymbol{\theta}^T\mathsf{A}\boldsymbol{\theta} = \|\mathsf{R}_{\boldsymbol{d}}\boldsymbol{\theta}\|^2 \geq 0$ for all $\boldsymbol{\theta}$ (A is *positive semidefinite* by construction), all eigenvalues of A will be non-negative. Thus, the maximizers will be those eigenvectors $\boldsymbol{v}_i$ of A with the largest eigenvalues. These are the special linear combinations, or groups, of basis bumps that we can use to minimize the radiative depolarization in the real accelerator. In our reduced space of only k knobs, we rewrite the least-squares problem as

$$\begin{aligned} -(\boldsymbol{f_d})_0 &= \mathsf{R}_{\boldsymbol{d}}(w_1\boldsymbol{v}_1 + ... + w_k\boldsymbol{v}_k) \\ \rightarrow \ -(\boldsymbol{f_d})_0 &= \tilde{\mathsf{R}}_{\boldsymbol{d}}\boldsymbol{w} \ , \end{aligned} \tag{84}$$

where $\tilde{\mathsf{R}}_{\boldsymbol{d}} = \mathsf{R}_{\boldsymbol{d}}\begin{pmatrix}\boldsymbol{v}_1 & \dots & \boldsymbol{v}_k\end{pmatrix}$ and $\boldsymbol{w} = (w_1, ..., w_k)^T$. In the ideal lattice, all we need to do now is calculate the least-squares solution to Eq. (84) to obtain the strengths for each of the composite bumps that minimize $\boldsymbol{d}$ in the bends.

In the real ring where random closed orbit distortions will degrade the spin match, we could just vary the strengths of these k bumps until the polarization is re-maximized.

4.2 Improving and Generalizing the Method

By doing a principal component analysis over the space of selected opposite π pairs in the ring, we thus far have a method to construct a minimal number of groups of basis bumps that have a *maximal* impact on the spin-orbit coupling. However, at the same time we would also like the groups to have a *minimal* impact on the orbit excursions, which the initial approach does not account for directly. Letting R_A specify the responses of the quantities we wish to maximally affect, and R_B specify the responses of those quantities we wish to minimally affect, we seek

$$\underset{\boldsymbol{\theta}_1,\ldots,\boldsymbol{\theta}_k}{\operatorname{argmax}} \frac{\|\mathsf{R}_A\boldsymbol{\theta}\|^2}{\|\mathsf{R}_B\boldsymbol{\theta}\|^2} = \underset{\boldsymbol{\theta}_1,\ldots,\boldsymbol{\theta}_k}{\operatorname{argmax}} \frac{\boldsymbol{\theta}^T\mathsf{A}\boldsymbol{\theta}}{\boldsymbol{\theta}^T\mathsf{B}\boldsymbol{\theta}} \,, \tag{85}$$

where $\mathsf{A} = \mathsf{R}_A^T\mathsf{R}_A$ and $\mathsf{B} = \mathsf{R}_B^T\mathsf{R}_B$. In this case, we would let $\mathsf{R}_A = \mathsf{R}_{\boldsymbol{d}}$ to maximally affect the spin-orbit coupling function at the bends, and $\mathsf{R}_B = \mathsf{R}_y$, where R_y is the response matrix of the vertical closed orbit at many positions around the ring, to minimally affect the closed orbit.

The quotient in Eq. (85) is called the *generalized Rayleigh quotient* of A, B, and $\boldsymbol{\theta}$, and we seek its maximizers. We once again follow the approach in [10]. Assuming that B is symmetric and *positive definite* such that $\boldsymbol{\theta}^T\mathsf{B}\boldsymbol{\theta} = \|\mathsf{R}_B\boldsymbol{\theta}\|^2 > 0$ for all $\boldsymbol{\theta}$, we can perform a Cholesky decomposition so that $\mathsf{B} = \mathsf{L}\mathsf{L}^T$. We then can rewrite the generalized Rayleigh quotient in Eq. (85) as

$$\frac{\boldsymbol{\theta}^T\mathsf{A}\boldsymbol{\theta}}{(\boldsymbol{\theta}^T\mathsf{L})(\mathsf{L}^T\boldsymbol{\theta})} = \frac{\tilde{\boldsymbol{\theta}}^T\mathsf{L}^{-1}\mathsf{A}\mathsf{L}^{-T}\tilde{\boldsymbol{\theta}}}{\tilde{\boldsymbol{\theta}}^T\tilde{\boldsymbol{\theta}}} \,, \quad \tilde{\boldsymbol{\theta}} = \mathsf{L}^T\boldsymbol{\theta} \,. \tag{86}$$

To calculate those $\tilde{\boldsymbol{\theta}}$ that maximize Eq. (86), the same Lagrangian as in Eq. (82) is obtained except with $\boldsymbol{\theta} \to \tilde{\boldsymbol{\theta}}$. Expressing this in terms of $\boldsymbol{\theta}$, we have

$$\mathcal{L} = \boldsymbol{\theta}^T\mathsf{A}\boldsymbol{\theta} + \lambda\left(\boldsymbol{\theta}^T\mathsf{B}\boldsymbol{\theta} - 1\right) \,. \tag{87}$$

Therefore, the problem of Eq. (85) is equivalently expressed as finding the maximizers of $\boldsymbol{\theta}^T\mathsf{A}\boldsymbol{\theta}$ subject to the constraint $\boldsymbol{\theta}^T\mathsf{B}\boldsymbol{\theta} = 1$. The stationary points of the Lagrangian are calculated as the solutions to

$$\frac{\partial\mathcal{L}}{\partial\boldsymbol{\theta}} = 2\mathsf{A}\boldsymbol{\theta} - 2\lambda\mathsf{B}\boldsymbol{\theta} = 0 \;\rightarrow\; \mathsf{A}\boldsymbol{\theta} = \lambda\mathsf{B}\boldsymbol{\theta} \,. \tag{88}$$

In this case, the generalized eigenvectors of A and B with largest eigenvalues define groups of basis bumps that have a *maximal* impact on the spin-orbit coupling, a *minimal* impact on the orbit, and, by choice of the basis bumps, have no delocalized transverse coupling nor delocalized vertical dispersion. For spin matching purposes, these groups are truly the "Best Adjustment Groups

for ELectron Spin" (BAGELS). We can use these BAGELS bumps to both optimally spin match the ideal ring via Eq. (84), and to optimally fix the spin match degradation caused by random closed orbit distortions in the real accelerator, by turning knobs that control these bumps in the control room. Being a more direct approach that also ensures minimal orbit excursions and no delocalized transverse coupling nor delocalized vertical dispersion, BAGELS effectively makes harmonic closed orbit spin matching obsolete for correcting polarization in operation.

When calculating the generalized eigenvectors on a computer, floating point roundoff errors caused by the potentially vastly different scales of R_A and R_B (e.g. the closed orbit responses being orders of magnitude smaller than the spin-orbit coupling responses) may affect the numerical solution. Therefore, in practice, the two matrices should be normalized to minimize this error. We use the matrix 2-norm so that $\bar{\mathsf{R}}_A = \mathsf{R}_A/\|\mathsf{R}_A\|$ and likewise for R_B. We then let $\mathsf{A} = \bar{\mathsf{R}}_A^T \bar{\mathsf{R}}_A$ and likewise for B.

In this generalized approach, the positive definiteness of B is required in order to obtain a solution. This is apparent by the fact that if B is only positive semidefinite and not positive definite, then an attempt at inversion/Cholesky decomposition of B to solve for the generalized eigenvectors in Eq. (88) will fail. In order to ensure $\boldsymbol{\theta}^T \mathsf{B} \boldsymbol{\theta} = \|\bar{\mathsf{R}}_B \boldsymbol{\theta}\|^2 > 0$ for all $\boldsymbol{\theta}$, all selected basis bumps must be orthogonal to each other - that is, no single selected basis bump should expressable as a linear combination of the other selected basis bumps. To construct an orthogonal basis for the opposite π pair basis bump, we sequentially choose as our basis bumps all opposite π pairs with a separation of only π in betatron phase advance between each of the bumps in a pair. With this choice, those opposite π pairs with separation $(2n+1)\pi,\ n \neq 1$ can be constructed as a linear combination of our orthogonal basis bumps.

While we have thus far shown how BAGELS is used to calculate the best vertical orbit bumps for spin matching purposes, the method is not limited to spin matching. BAGELS can also be applied in applications where a *minimal* impact on polarization is desired, amongst other things; suppose we instead would like to calculate bumps that maximally change some other quantity x around the ring, but minimally impact both the spin-orbit coupling and the closed orbit excursions. To calculate such bumps, we can combine the responses of the spin-orbit coupling function and the orbit excursions into the response matrix $\bar{\mathsf{R}}_B$ (properly normalized), let $\bar{\mathsf{R}}_A = \mathsf{R}_x/\|\mathsf{R}_x\|$, and then choose those eigenvectors with the largest eigenvalues. This approach is used to calculate "polarization-safe" bumps to optimally correct global coupling in Sec. 5.2, and "polarization-safe" vertical emittance creation bumps for beam size matching in Sec. 5.3. Finally, while it is not explored in this paper, the basis vectors of the "groups" do not need to be vertical orbit bumps, but could instead be single corrector coil strengths, or some other magnet strengths, for example. The only requirement is that a sufficiently linear relationship exists between the input and output, and that the input forms an orthogonal basis. With such generality, BAGELS allows for computation of the "Best Adjustment Groups for ELectron Spin" in any application.

In summary, to apply BAGELS:

1. **Choose the basis bumps/vectors:** The choice of basis vectors should be guided by the goal. For spin matching, every orthogonal opposite π pair, which creates neither delocalized vertical dispersion nor delocalized coupling, is ideal. In Sec. 5.2 and Sec. 5.3 we define two different types of useful basis vectors for different applications.

2. **Construct the response matrices:** All quantities in consideration must have a sufficiently linear relationship with the basis vectors. When combining the response matrices of multiple quantities into either R_A or R_B, each submatrix may also be normalized to weigh the treatment of the different responses.

3. **Calculate the generalized eigenvectors of the covariance matrices to obtain the Best Adjustment Groups for ELectron Spin:** The best groups will be those eigenvectors with the largest eigenvalues for maximal/minimal impact on polarization.

5 BAGELS Results

5.1 Spin Match the Ideal Ring

5.1.1 1-IP 18 GeV EIC-ESR

To apply BAGELS in the ideal 1-IP 18 GeV EIC-ESR, we use an orthogonal basis consisting of opposite π pairs in the four arcs surrounding the spin rotator, two on either side. With radiation damping turned off, we calculate for each basis bump the responses of $\boldsymbol{d}\sqrt{L|\boldsymbol{g}|^3}$ at the ends of each bend (which we aim to maximize), as well as the vertical orbit y at many positions around the ring (which we aim to minimize). Specifically, we sampled the ends of every lattice element (all drifts, quadrupoles, sextupoles, bends, solenoids) for y. Henceforth for notational brevity, $\mathsf{R}_{\boldsymbol{d}}$ denotes the response matrix of $\boldsymbol{d}\sqrt{L|\boldsymbol{g}|^3}$ at all bends. We compute the top four maximizers of Eq. (85), and use them as our knobs to achieve a spin match. Finally, in this reduced space of only four knobs, we solve Eq. (84) for the least-squares solution to obtain the strengths of the four knobs in the ideal lattice. The before-and-after result is shown in Fig. 11, with the interaction point at $s = 0$ m.

The radiation damping will cause a "sawtooth" closed orbit, which must be corrected. Because we use the 1-IP ESR lattice for the random error studies in Sec. 5.2, we use the proposed orbit correction scheme for the ring at the time of paper writing to correct the sawtooth closed orbit. This consists of dual plane BPMs and vertical corrector coils at each vertically-focusing quadrupole outside of the interaction region, and horizontal corrector coils at each horizontally-focusing quadrupole outside of the interaction region. In the interaction region, dual plane BPMs and dual plane correctors are used at each quadrupole.

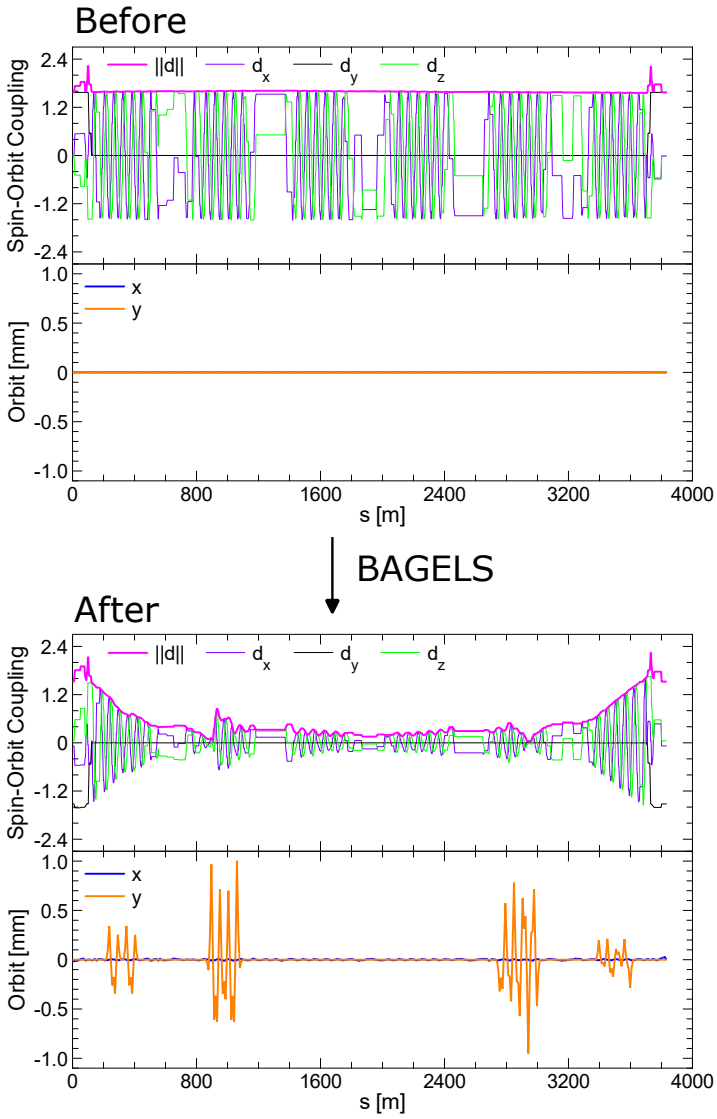

Figure 11: The spin-orbit coupling function $\boldsymbol{d}$ and closed orbit in the ideal 1-IP 18 GeV EIC-ESR before (top) and after (bottom) applying BAGELS, using only four BAGELS vertical orbit bumps. The interaction point at the center of the spin rotator shown in Fig. 2 is located at $s = 0$ m.

The RMS closed orbit was then minimized using the *Tao* program in the *Bmad* ecosystem.

Figure 12 shows an energy scan of P_{dk} of the 1-IP ESR before and after ap-

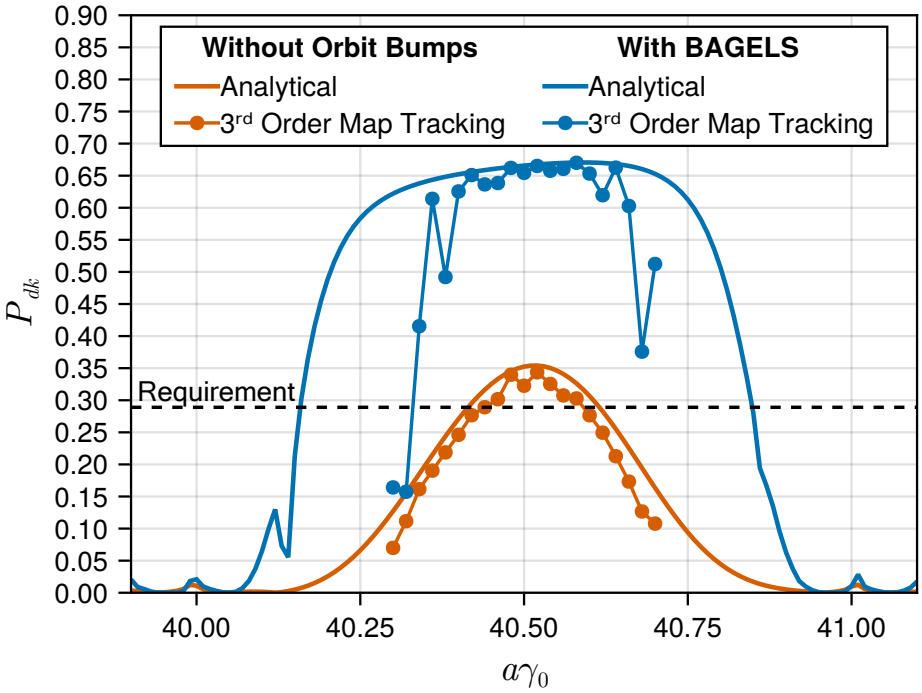

Figure 12: An energy scan of the asymptotic polarization in the ideal 1-IP 18 GeV EIC-ESR, both before and after applying BAGELS. Using only four BAGELS vertical orbit bumps, the asymptotic polarization is nearly doubled in nonlinear tracking.

plying BAGELS. Note that polarized bunches will be injected into the ESR, and then replaced once sufficiently depolarized. The "Requirement" line shows the minimum allowable P_{dk} in order to ensure a time-averaged polarization of 70% is maintained. Using only four BAGELS bumps, which create a maximum orbit excursion of ≈ 1 mm, we nearly double the asymptotic polarization.

We could have alternatively used only two of the arcs surrounding the IP instead of four, and similarly achieved a good solution. However, the orbit excursions must grow larger in order to solve Eq. (84) for the least-squares solution, whereas with four arcs the orbit excursions are minimal.

We remark that because this is the ideal ring (no random closed orbit distortions causing any tilts to $\hat{\boldsymbol{n}}_0$), the "Without Orbit Bumps" case in Fig. 12 has a *full harmonic closed orbit spin match already*. HCOSM therefore cannot improve this case, even though it is clearly suboptimal. This result shows that, for the general case where the spin rotator may not have a full strong synchrobeta spin match, as in the EIC-ESR, tilts to $\hat{\boldsymbol{n}}_0$ can actually be hugely beneficial, and that BAGELS can be used to directly find the optimal solution, while HCOSM

would lead away from the optimal solution.

5.1.2 2-IP 18 GeV EIC-ESR

In the 2-IP ESR, both interaction points including spin rotators are separated by one periodic arc section. To spin match this lattice, we use an orthogonal basis consisting of opposite π pairs in the four arcs surrounding both spin rotators, i.e. two arcs upstream of the first spin rotator and two arcs downstream the second spin rotator. Once again applying BAGELS, with radiation damping turned off we calculate the responses of $\boldsymbol{d}\sqrt{L|\boldsymbol{g}|^3}$ at the ends of each bend and of the vertical orbit y at the ends of each element. We compute the top four maximizers of Eq. (85), and use them to solve for a least-squares solution to Eq. (84). Figure 13 shows the spin-orbit coupling function and closed orbit after applying BAGELS to the ideal 2-IP 18 GeV ESR.

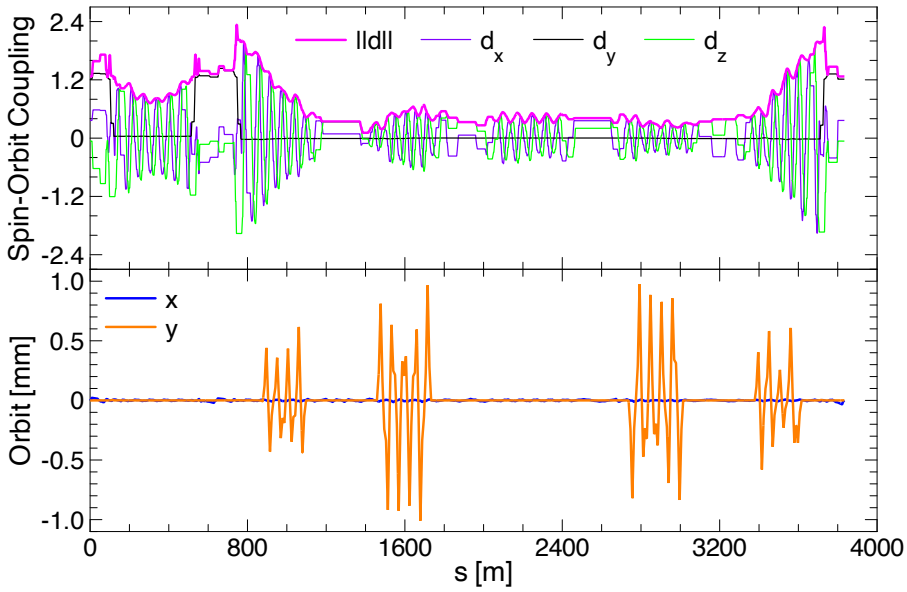

Figure 13: The spin-orbit coupling function $\boldsymbol{d}$ and closed orbit in the ideal 2-IP 18 GeV EIC-ESR before after applying BAGELS, using only four BAGELS vertical orbit bumps. The IPs at the center of the spin rotators (each shown in Fig. 2) are located at s = 0 m and s = 640.758 m.

Unlike the 1-IP lattice in this manuscript, to correct the sawtooth closed orbit caused by radiation damping in the 2-IP lattice we use the `taper` command in the *Tao* program; this command provides a quick-and-dirty solution by varying all magnet strengths in the ring proportionally to the local closed orbit momentum deviation. In reality, however, the ESR will not use tapering

to correct the sawtooth. To ensure accuracy, we compared using `taper` vs. a proper orbit correction in the 1-IP lattice, and did not observe a significant difference in the tracking results.

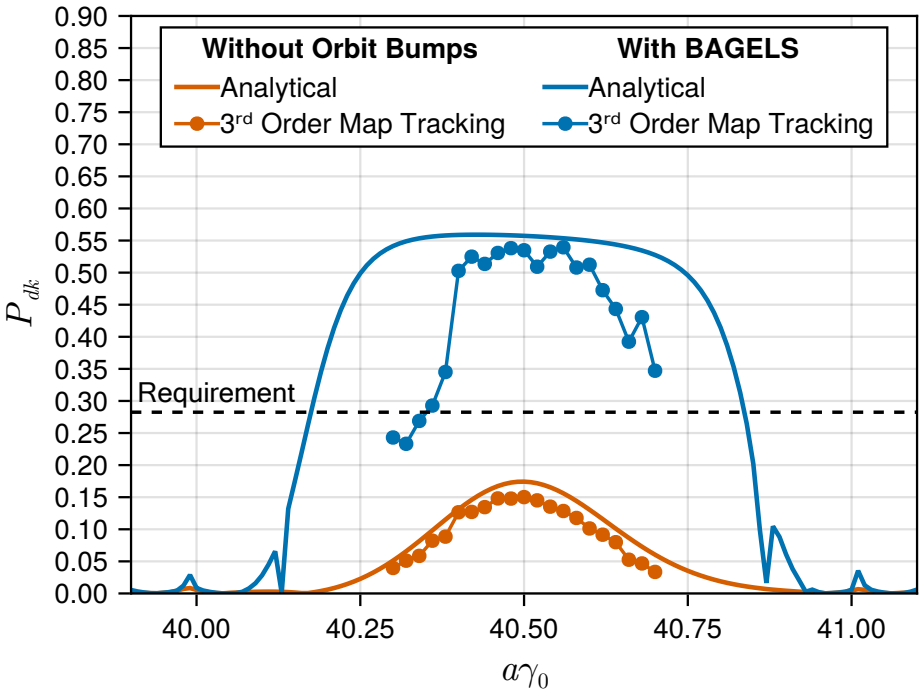

Figure 14: An energy scan of the asymptotic polarization in the ideal 2-IP 18 GeV EIC-ESR, both before and after applying BAGELS. Using only four BAGELS vertical orbit bumps, the asymptotic polarization is more than tripled in nonlinear tracking.

Figure 14 shows an energy scan of P_{dk} of the 2-IP ESR before and after applying BAGELS. Using only four BAGELS bumps, which create a maximum orbit excursion of $\approx$ 1 mm, we more than triple the asymptotic polarization. Before BAGELS, the 2-IP 18 GeV ESR does not provide the sufficient time-averaged polarization at the interaction points [20]. After application of BAGELS, the polarization requirements are exceeded.

5.2 Random Errors and Global Coupling Correction

In the real ring, the BAGELS spin matching knobs can be used to optimally restore the spin match degradation caused by random closed orbit distortions. However before this is done, the global, delocalized transverse coupling caused by the random errors must be corrected. One way to do so is by using verti-

cal orbit bumps through the sextupoles to create coupling that cancels out the coupling caused by the random errors. By applying BAGELS, we can compute a minimal number of such bumps which maximally, and orthogonally, impact the coupling, while minimally impacting the spin-orbit coupling function and creating minimal orbit excursions.

We use the coupling formalism defined in [18]. The 1-turn transverse transport matrix is decomposed as

$$\mathsf{M}_{4\times4} = \mathsf{G}^{-1}\bar{\mathsf{V}}\bar{\mathsf{U}}\bar{\mathsf{V}}^{-1}\mathsf{G}\,, \tag{89}$$

$$\mathsf{G} = \begin{pmatrix} \mathsf{G}_a & 0 \\ 0 & \mathsf{G}_b \end{pmatrix},\ \bar{\mathsf{V}} = \begin{pmatrix} \chi\mathsf{1} & \bar{\mathsf{C}} \\ -\bar{\mathsf{C}}^{+} & \chi\mathsf{1} \end{pmatrix},\ \bar{\mathsf{U}} = \begin{pmatrix} \bar{\mathsf{U}}_a & 0 \\ 0 & \bar{\mathsf{U}}_b \end{pmatrix},$$

where G is a linear normalizing transformation (i.e. G_a and G_b are Courant-Snyder transformations up to a rotation of the "a" and "b" modes), $\bar{\mathsf{V}}$ is a symplectic matrix that defines the amount of coupling between the transverse planes (where the + denotes the symplectic conjugate), and $\bar{\mathsf{U}}$ is an uncoupled rotation. In order to ensure the symplecticity of $\bar{\mathsf{V}}$, we demand $\chi^2 + \det(\bar{\mathsf{C}}) = 1$. If there is no transverse coupling, then $\chi = 1$, $\bar{\mathsf{C}} = 0$, and the "a" mode corresponds to the horizontal and the "b" mode the vertical. The matrix $\bar{\mathsf{C}}$ is referred to as the *normalized coupling matrix*, and provides a good measure of the coupling at a point in the ring.

We apply BAGELS seeking groups that maximally impact the normalized coupling matrix components $\bar{\boldsymbol{C}} = (\bar{C}_{11}, \bar{C}_{12}, \bar{C}_{21}, \bar{C}_{22})^T$ at each element in the ring, while minimally impacting both the spin-orbit coupling function at the bends and the orbit excursions at all elements. Following the recipe at the end of Sec. 4.2, we first must choose a basis bump. Ideally, we choose a bump that generates delocalized transverse coupling, but no delocalized vertical dispersion. Taking advantage of the periodic layout of the sextupole families in the arcs, two equivalent π bumps directly next to each other, as shown in Fig. 15, is exactly such a basis bump. By sequentially choosing each equal π pair in each arc, we obtain an orthogonal basis about which to construct our BAGELS global coupling correction knobs.

Next, we must construct the response matrices. Following the notation in Eq. (85), we use

$$\mathsf{R}_A = \mathsf{R}_{\bar{\boldsymbol{C}}},\ \mathsf{R}_B = \begin{pmatrix} \mathsf{R}_{\boldsymbol{d}}/\|\mathsf{R}_{\boldsymbol{d}}\| \\ \mathsf{R}_y/\|\mathsf{R}_y\| \end{pmatrix} \tag{90}$$

to calculate bumps that maximally impact the coupling matrix components but minimally impact both the orbit and the spin-orbit coupling function. Here, the submatrix normalizations serve an important purpose. The different responses may be multiplied by any arbitrary scalars to give a greater/lesser weight to those responses in the eigenvector calculation. To ensure equal treatment of all responses, we choose to normalize each submatrix by its 2-norm. This is now in addition to minimizing the floating point roundoff errors caused by the potentially vastly different scales.

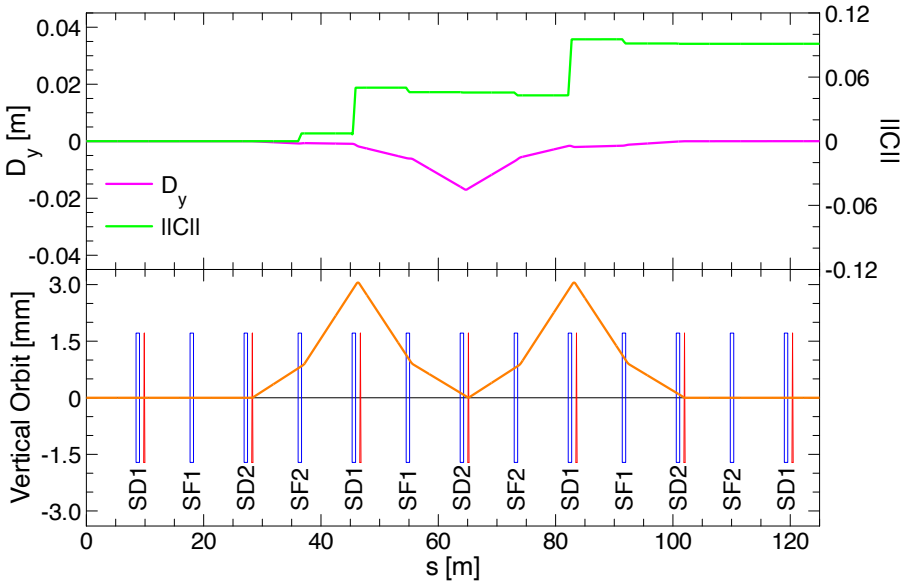

Figure 15: Equal π pair placed in a periodic FODO beamline with 90° phase advance per cell and two sextupole families per plane (SF for the horizontal, SD for the vertical). Sextupoles are specified as blue rectangles, vertical corrector coils as red triangles, and the quadrupoles and bends are not shown. The bump's corresponding vertical dispersion D_y and normalized coupling matrix norm $\|\bar{C}\|$ are plotted above [18]. The equal π pair creates delocalized transverse coupling but localized vertical dispersion.

Finally, we compute the generalized eigenvectors and obtain the BAGELS bumps for global coupling correction via vertical orbits through the sextupoles. We chose only the top four BAGELS bumps for optimal, polarization-safe coupling correction. Knobs that control these bumps could be varied freely to correct the coupling, with minimal impacts on both the polarization and the closed orbit. BAGELS allows for the decoupling (no pun intended) of global coupling compensation and the polarization.

To test the efficacy of both the four BAGELS global coupling correction knobs and the four BAGELS spin matching knobs including random closed orbit distortions, we generated 10 1-IP ESR lattices with different error seeds using the RMS errors shown in Table 5.

After first minimizing the RMS orbit for each seed using the orbit correction scheme outlined in Sec. 5.1.1, we varied the four BAGELS global coupling correction knobs until the RMS normalized coupling matrix components at each BPM were minimized. Then after resetting the tunes of the ring to their design

Table 5: RMS Errors used in the Random Errors Study

RMS Error	x [mm]	y [mm]	Roll [mrad]	$\Delta B/B$ [%]
Dipoles	0.2	0.2	0.5	0.1
Quadrupoles	0.2	0.2	0.5	0.1
Sextupoles	0.2	0.2	0.5	0.2
High-β Dipoles	0.2	0.2	0.5	0.05
Final Focus Quads	0.1	0.1	0.5	0.05

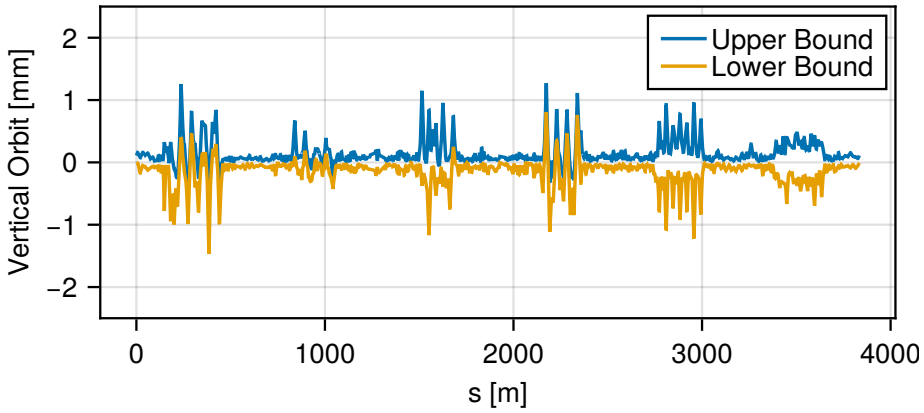

Figure 16: Upper and lower bounds of the vertical closed orbit across 10 error seeds of the 1-IP 18 GeV EIC-ESR after orbit correction, coupling correction using four BAGELS global coupling correction bumps, and spin match restoration using four BAGELS spin matching bumps. The IP is located at $s = 1277.948$ m.

values using the arc quadrupoles, the four BAGELS spin matching knobs were varied until the polarization was maximized. Figure 16 shows the upper and lower bounds of the vertical orbits for the 10 seeds after the full correction.

One good measure of the transverse coupling around the ring is the "vertical-like" equilibrium eigenemittance ϵ_b, as calculated in [29]; if the transverse coupling has been sufficiently corrected, then ϵ_b should be restored to a value much smaller than the horizontal-like emittance. Therefore, to measure the efficacy of the BAGELS transverse coupling correction knobs, we use the vertical-like eigenemittance ϵ_b as our figure-of-merit. In all cases, the analytical (first-order) ϵ_b was reduced to < 0.61 nm. The analytical (first-order) P_{dk} for all errors seeds was $\geq 55\%$, with the average analytical P_{dk} amongst all 10 seeds equal to 62.7%.

We now describe the results of nonlinear tracking for each seed. Figure 17 shows an energy scan of the resulting asymptotic polarizations and mean $\epsilon_{b,RMS}$ obtained from 3$^{\text{rd}}$ order map tracking for each seed. For all 10 error seeds, the polarization requirements for the 1-IP ESR are well exceeded. For two of the

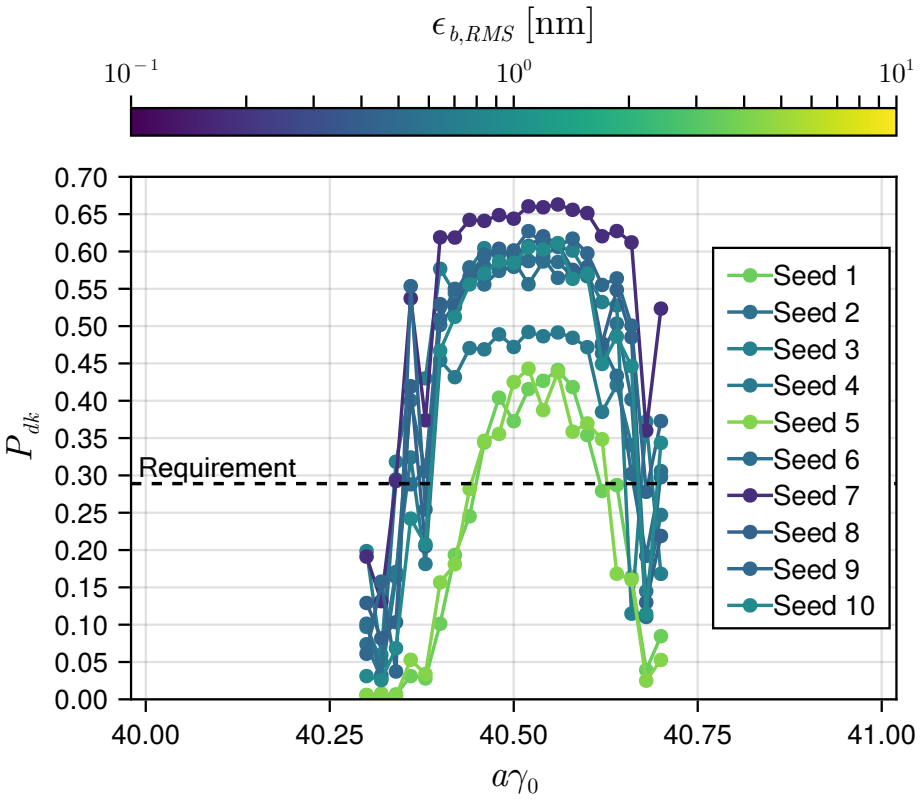

Figure 17: A 3[rd] order map tracking energy scan of the asymptotic polarizations in 10 different 1-IP 18 GeV EIC-ESR lattices including the RMS errors listed in Table 5. Four BAGELS global coupling correction knobs were used to correct the coupling, followed by four BAGELS spin matching knobs to restore the spin match. The line colors correspond to the vertical-like mean equilibrium eigenemittance obtained in tracking for each seed.

error seeds, linear coupling correction does not result in a sufficient reduction of the nonlinear vertical emittance. While nonlinear emittance control is not the topic of this paper, it is remarkable that even in these cases BAGELS leads to sufficient P_{dk} to achieve the polarization goals of the ESR. For 7 of the 10 seeds, asymptotic polarizations of $\approx$ 60% or more are achieved while having vertical equilibrium emittances in nonlinear tracking that agree very well with their linear calculations, suggesting excellent coupling control. For the two seeds with lower asymptotic polarization and a nonlinear $\epsilon_{b,RMS}$ increase, it is likely that a further optimization of the chromatic solution and/or harmonic sextupoles may gain control of the nonlinear $\epsilon_{b,RMS}$ and obtain a corresponding increase in P_{dk}. In this case, because the BAGELS transverse coupling correc-

tion knobs rely on the sextupole strengths, some iteration will be required for an optimal solution. Overall, these results suggest that the four BAGELS spin matching bumps are highly efficacious and robust against random closed orbit distortions, and that the four BAGELS global coupling correction bumps can be used for excellent polarization-safe coupling control.

5.3 Vertical Emittance Creation

In order to achieve maximum luminosity in the EIC, the beam sizes of the electron and hadron beams must be matched. Because of radiation damping, the electron beam vertical emittance will be approximately zero, and if the vertical dispersion at the IP is to be kept to zero, then the vertical emittance must be intentionally increased in order to achieve a beam size match, specifically $\epsilon_y \approx 2$ nm. However, a nonzero vertical emittance is notoriously bad for electron polarization, and without a careful approach is all but guaranteed to significantly reduce the asymptotic polarization.

There are many different ways to generate vertical emittance. One way is to use a large vertical chicane as a local vertical dispersion bump, so that a vertical amplitude is excited when photons are emitted in the chicane. This was attempted in the ESR, however to achieve the necessary emittance the chicane requires too strong magnetic fields, geometrically is extremely challenging to fit in the ring, and degrades the spin match significantly [23]. Alternatively, a localized region with a large amount of coupling where photons are emitted may be used to effectively "couple" part of the horizontal emittance into the vertical. However this has not been investigated in-depth, and will also certainly degrade the spin match significantly without a careful approach.

Instead of a localized approach, vertical emittance could be created by using vertical orbit bumps that either (1) generate delocalized transverse coupling via the skew quadrupole feed-down term in the sextupoles, or (2) generate delocalized vertical dispersion, caused by the corrector coils themselves, so that photon emission causes a vertical amplitude excitation. We investigate both such approaches using BAGELS. We also investigate a third approach where, using BAGELS, delocalized vertical dispersion is generated while simultaneously matching the dispersion to zero at the IP.

5.3.1 Delocalized Transverse Coupling

The BAGELS global coupling correction bumps we calculated in Sec. 5.2 have a maximum impact on the normalized coupling matrix components around the ring, a minimal impact on both the spin-orbit coupling function and the orbit, and by design create no delocalized vertical dispersion. This makes the BAGELS coupling correction bump with the largest eigenvalue perfect for creating vertical emittance via a delocalized transverse coupling wave. In the ideal 1-IP ESR, we simply turned this knob until the linear $\epsilon_b \approx 2$ nm.

The working point of this ESR lattice is $(Q_x, Q_y, Q_s) = (0.08, 0.14, 0.05)$. Interestingly, we found in nonlinear tracking that delocalized coupling readily

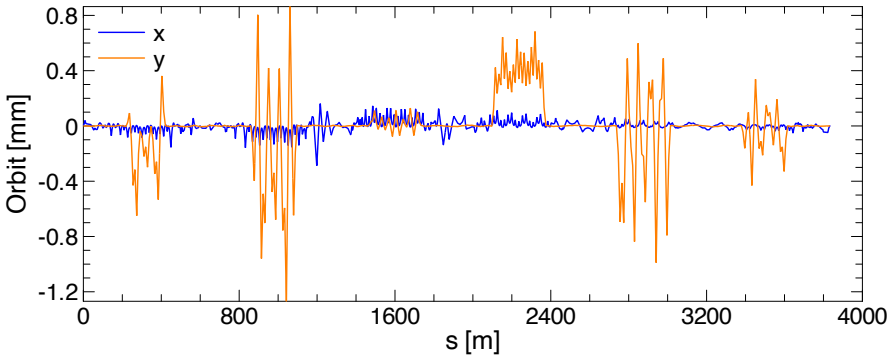

Figure 18: Closed orbit in a 1-IP 18 GeV EIC-ESR after using a single BAGELS coupling-creation bump to generate sufficient vertical emittance for beam size matching. The small horizontal orbit is due to radiation damping. The IP is located at $s = 0$ m.

excited the $Q_y - Q_x - Q_s$ resonance, causing an uncontrolled vertical emittance increase. Because the correction of this effect is not the topic of this paper, we adjusted the working point slightly to $(0.08, 0.15, 0.045)$ by varying the arc quadrupoles and RF cavity voltages, to move away from this resonance.

We observed essentially zero impact on the analytical polarization after adjusting the BAGELS coupling-creating knob for linear $\epsilon_b \approx 2$ nm; only miniscule adjustments to the four BAGELS spin matching bumps were needed to re-maximize the analytical polarization. The closed orbit after using the BAGELS bumps is shown in Fig. 18.

As shown in the energy scan in Fig. 19, using one BAGELS coupling-creation bump and four BAGELS spin matching bumps, polarization requirements are well exceeded while simultaneously achieving sufficient vertical emittance in nonlinear tracking, even with a small nonlinear increase in ϵ_b. The disagreement of the analytical polarization calculation with nonlinear tracking is not surprising; the spin-orbit coupling function can vary significantly with the vertical orbital amplitude, and the analytical calculation only evaluates the spin-orbit coupling function on the closed orbit.

5.3.2 Delocalized Vertical Dispersion

Using the coupling formalism as in Sec. 5.2, we can define a- and b-mode periodic dispersions as

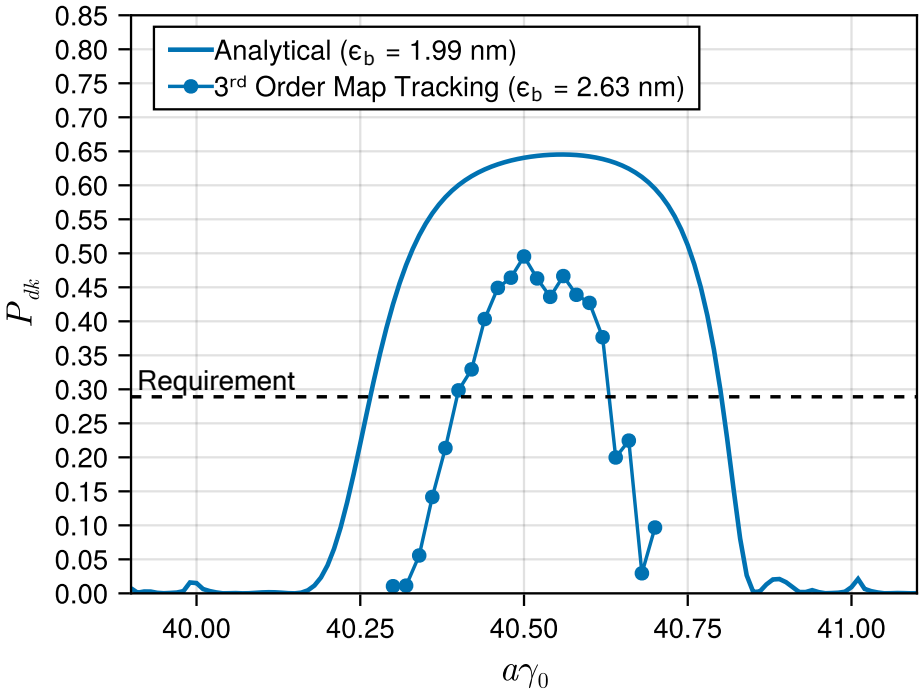

Figure 19: An energy scan of the asymptotic polarization in the ideal 1-IP 18 GeV EIC-ESR after using a single BAGELS coupling-creation bump to set the analytical vertical emittance to 1.99 nm. The disagreement of the analytical calculation with nonlinear tracking is expected because the phase space dependence of the spin-orbit coupling function, which can vary significantly in the vertical, is neglected in the analytical calculation.

$$\begin{pmatrix} \eta_a \\ \eta'_a \\ \eta_b \\ \eta'_b \end{pmatrix} = \mathsf{G}^{-1}\bar{\mathsf{V}}^{-1}\mathsf{G}\begin{pmatrix} \eta_x \\ \eta'_x \\ \eta_y \\ \eta'_y \end{pmatrix} . \tag{91}$$

The excitation of a "b"-mode (vertical-like) amplitude caused by photon emission is directly characterized by

$$\mathcal{H}_b = \bar{\eta}_{b1}^2 + \bar{\eta}_{b2}^2 , \quad \bar{\eta}_{b1} = \frac{\eta_b}{\sqrt{\beta_b}} , \; \bar{\eta}_{b2} = \frac{\alpha_b\eta_b + \beta_b\eta'_b}{\sqrt{\beta_b}} , \tag{92}$$

in places where photons are emitted [19, 17]. The Twiss parameters are defined by the Courant-Snyder form of G_b. Thus, to generate vertical emittance by radiation in areas where a vertical amplitude is excited, we seek a single

BAGELS bump that maximally impacts $\mathcal{H}_b$ in the bends, but minimally impacts the spin-orbit coupling function in the bends and the orbit in all elements. The bump should also by construction generate no delocalized transverse coupling.

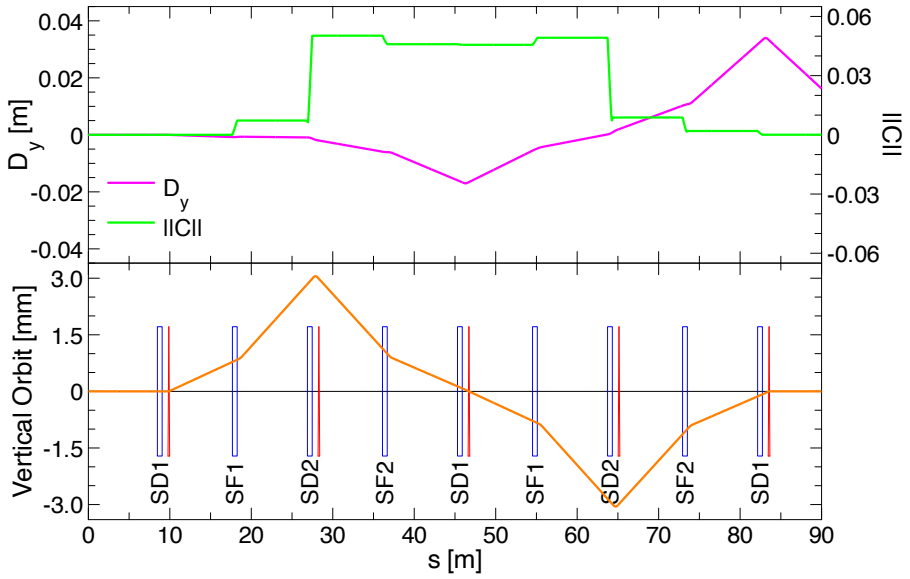

Figure 20: 2π bump placed in a periodic FODO beamline with 90° phase advance per cell and two sextupole families per plane (SF for the horizontal, SD for the vertical). Sextupoles are specified as blue rectangles, vertical corrector coils as red triangles, and the quadrupoles and bends are not shown. The bump's corresponding vertical dispersion D_y and normalized coupling matrix norm $||\tilde{C}||$ are plotted above [18]. The 2π bump creates delocalized vertical dispersion but localized coupling.

Once again, we follow the recipe at the end of Sec. 4.2. First, we need to choose a basis bump. To cancel the coupling created by a single π bump in a periodic FODO section, we need to place an opposite π bump positioned πn away in betatron phase. For the "opposite π pair" we used for spin matching, we positioned the second bump exactly π away from the first, to cancel both the coupling and vertical dispersion. In this case, we want to coherently build vertical dispersion while cancelling the coupling, so instead we can place the second π bump $2\pi n$ away from the first in betatron phase. To construct an orthogonal basis fully spanning the space, we position the second directly following the first so that $n = 0$, and sequentially select all such combinations in each arc. We refer to this basis bump, shown in Fig. 20, as a "2π bump" for the

obvious reason. The 2π bump, which generates delocalized vertical dispersion but no delocalized coupling, is the perfect basis bump to use for generating vertical emittance via delocalized vertical dispersion.

Now that we have chosen a basis bump, we must construct the response matrices. One of the requirements for BAGELS to work is a sufficiently linear dependence of the quantities with the basis vectors. In this case, $\mathcal{H}_b$ does not vary linearly with the 2π bump strength, however $\bar{\eta}_{b1}$ and $\bar{\eta}_{b2}$ do. Following the notation in Eq. (85), for a maximal impact on $\bar{\eta}_{b1}$ and $\bar{\eta}_{b2}$ with a minimal impact on the spin-orbit coupling function $\boldsymbol{d}$ and the orbit y we use

$$\mathsf{R}_A = \mathsf{R}_{(\bar{\eta}_{b1},\bar{\eta}_{b2})}\ ,\ \mathsf{R}_B = \begin{pmatrix} \mathsf{R}_{\boldsymbol{d}}/\|\mathsf{R}_{\boldsymbol{d}}\| \\ \mathsf{R}_y/\|\mathsf{R}_y\| \end{pmatrix}, \tag{93}$$

to calculate bumps that maximally impact $\mathcal{H}_b$ and minimally impact the spin-orbit coupling and orbit. Finally, we use the one group with largest eigenvalue as our polarization-safe vertical dispersion creation bump, and vary that until $\epsilon_b \approx 2$ nm in the analytical calculation. Varying the BAGELS vertical dispersion creation bump caused essentially no changes to the polarization; only miniscule changes to the BAGELS spin matching knobs were made to re-maximize the analytical polarization. The closed orbit after using the BAGELS bumps is shown in Fig. 21.

Figure 22 shows an energy scan of the asymptotic polarization using the one BAGELS vertical dispersion creation bump for beam size matching. Excellent polarization, well exceeding the requirement, is achieved while simultaneously creating sufficient vertical emittance in nonlinear tracking. Just as with the delocalized coupling creation method in Sec. 5.3.1, only a small nonlinear increase in ϵ_b was observed, and with BAGELS the polarization requirements

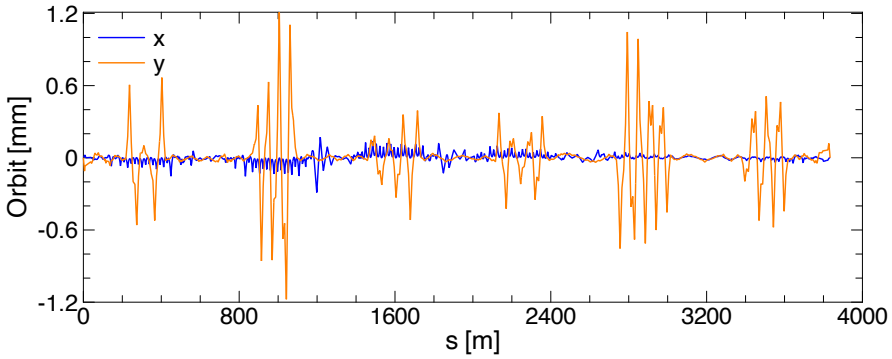

Figure 21: Closed orbit in a 1-IP 18 GeV EIC-ESR after using a single BAGELS vertical dispersion-creation bump to generate sufficient vertical emittance for beam size matching. The small horizontal orbit is due to radiation damping. The IP is located at $s = 0$ m.

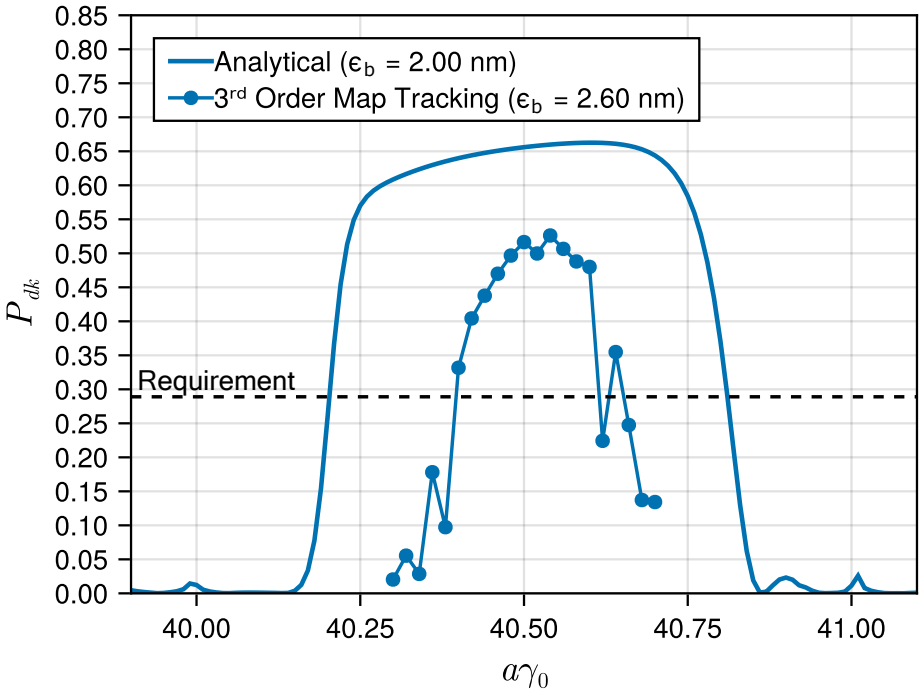

Figure 22: An energy scan of the asymptotic polarization in the ideal 1-IP 18 GeV EIC-ESR after using a single BAGELS vertical dispersion-creation bump to set the analytical vertical emittance to 2.00 nm. The disagreement of the analytical calculation with nonlinear tracking is expected because the phase space dependence of the spin-orbit coupling function, which can vary significantly in the vertical, is neglected in the analytical calculation.

are still well-exceeded. Because the BAGELS vertical dispersion-creating bump does not require any change to the working point of the lattice to avoid nonlinear resonances, this method is recommended for polarization-safe beam size matching in the EIC-ESR.

5.3.3 Delocalized Vertical Dispersion with IP Match

The BAGELS bump in Sec. 5.3.2 simultaneously (1) achieves sufficient vertical emittance via a delocalized vertical dispersion wave, (2) has minimal impacts to the polarization and orbit, and (3) generates no delocalized transverse coupling by use of 2π bumps as the basis bumps. However, it does not ensure the vertical dispersion and vertical dispersion slope is set to zero at the IP. To include this requirement in the BAGELS solution, we simply include η_b and η'_b at the IP in the response matrix of quantities to minimally affect. Once again

using the 2π bump as the basis bump, and following the notation in Eq. (85), we perform BAGELS using

$$\mathsf{R}_A = \mathsf{R}_{(\bar{\eta}_{b1},\bar{\eta}_{b2})}\ ,\ \mathsf{R}_B = \begin{pmatrix} \mathsf{R}_d/\|\mathsf{R}_d\| \\ \mathsf{R}_y/\|\mathsf{R}_y\| \\ \mathsf{R}_{\eta_b,IP}/\|\mathsf{R}_{\eta_b,IP}\| \\ \mathsf{R}_{\eta'_b,IP}/\|\mathsf{R}_{\eta'_b,IP}\| \end{pmatrix}, \tag{94}$$

where $\mathsf{R}_{\eta_b,IP}$ and $\mathsf{R}_{\eta'_b,IP}$ specify the responses of η_b and η'_b at the IP for each 2π bump respectively. The resulting group with the largest eigenvalue defines a BAGELS bump that achieves all the effects of the bump in Sec. 5.3.2, *while also ensuring minimal impacts to the dispersion at the IP*; the bump can be varied to create a polarization-safe delocalized vertical dispersion wave that automatically cancels itself at the IP.

The BAGELS bump was varied so that the analytical $\epsilon_b \approx 2$ nm, and the four BAGELS spin matching bumps were varied to re-maximize the analytical

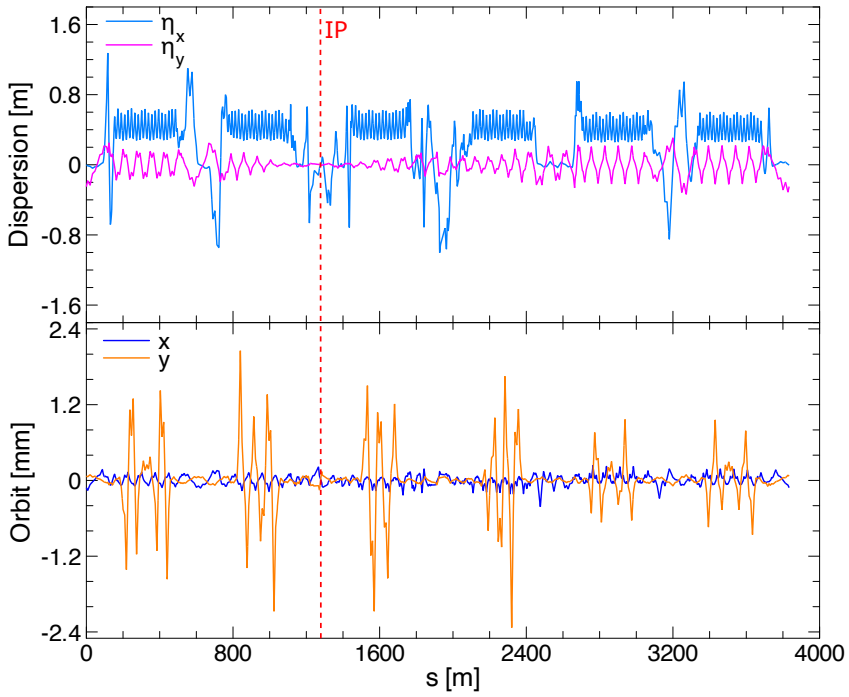

Figure 23: Dispersion and closed orbit in a 1-IP 18 GeV EIC-ESR after using a single BAGELS simultaneous vertical dispersion-creation and IP dispersion matching bump to generate sufficient vertical emittance for beam size matching. The small horizontal orbit is due to radiation damping. The IP is located at $s = 1277.948$ m and is denoted by the red dashed line.

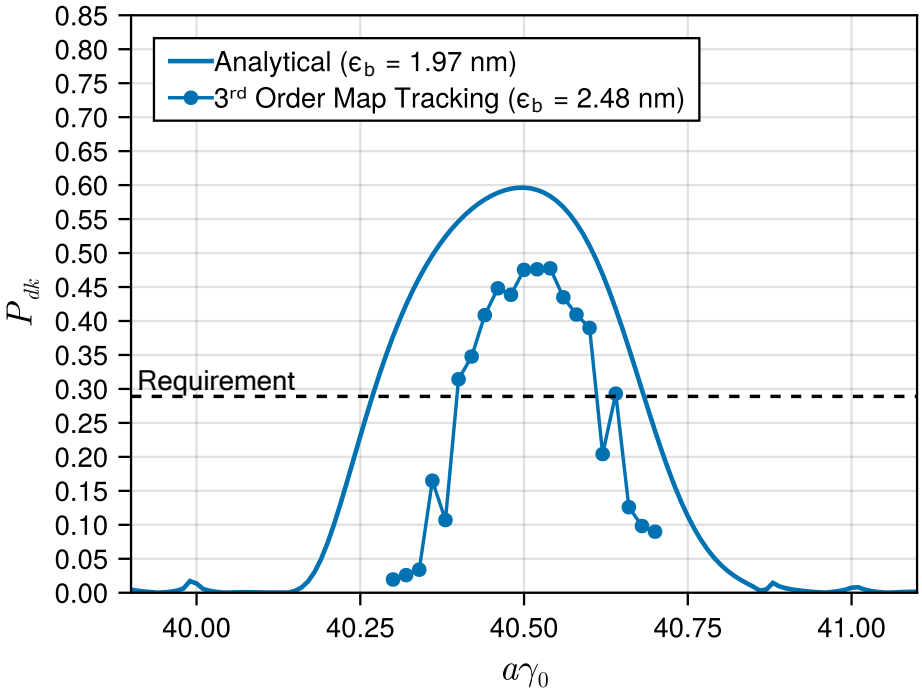

Figure 24: An energy scan of the asymptotic polarization in the ideal 1-IP 18 GeV EIC-ESR after using a single BAGELS simultaneous vertical dispersion-creation and IP dispersion matching bump to set the analytical vertical emittance to 1.97 nm. The disagreement of the analytical calculation with nonlinear tracking is expected because the phase space dependence of the spin-orbit coupling function, which can vary significantly in the vertical, is neglected in the analytical calculation.

polarization. The periodic dispersion and closed orbit after using the BAGELS bumps are shown in Fig. 23. As shown, the BAGELS bump maintains the dispersion match at the IP.

Figure 24 shows an energy scan of the asymptotic polarization using the one BAGELS simultaneous vertical dispersion-creation and IP dispersion matching bump. Remarkably, while the analytical polarization is slightly deteriorated when compared with the unmatched-IP BAGELS bump in Sec. 5.3.2, the polarization obtained in nonlinear tracking shows very similar performance; the polarization requirements are well exceeded, and only a small nonlinear increase in ϵ_b was observed.

5.4 Conclusions

Best Adjustment Groups for ELectron Spin (BAGELS) provides a rigorous framework to construct a minimal number of control parameter groups, or knobs, that have optimal impacts on the radiative depolarization, orbit, and optics. For spin matching purposes, we used BAGELS to compute special vertical orbit bumps, each a linear combination of basis bumps, that maximally affect the radiative depolarization around the ring while creating minimal orbit excursions and no delocalized vertical dispersion nor delocalized coupling. The BAGELS spin matching bumps work by intentionally tilting $\hat{\boldsymbol{n}}_0$ to create spin-orbit coupling which can be used to cancel the spin-orbit coupling in the ring, e.g. caused by spin rotators or random errors. For the design of the EIC-ESR, we used only four BAGELS spin matching knobs to significantly increase the asymptotic polarizations in nonlinear trackings of the 1- and 2-IP 18 GeV lattices, almost doubling P_{dk} in the former and more than tripling P_{dk} in the latter. For the EIC-ESR we also applied BAGELS in various applications where a minimal impact on polarization was desired: first, we calculated four BAGELS vertical orbit bumps that can be used to maximally correct the global transverse coupling caused by random errors, while minimally impacting the orbit and radiative depolarization. We then tested both these four BAGELS transverse coupling correction knobs and the four BAGELS spin matching knobs for 10 different error seeds in the 1-IP 18 GeV EIC-ESR, and showed excellent simultaneous polarization and transverse coupling control. Secondly, we calculated three different types of vertical emittance creation knobs that can each be varied with truly minimal impacts to the radiative depolarization and orbit: one that creates delocalized coupling, one that creates delocalized vertical dispersion, and one that creates delocalized vertical dispersion while maintaining a dispersion match at the IP. All knobs showed excellent simultaneous polarization and vertical emittance control in nonlinear tracking. BAGELS has solved the challenges of simultaneously maximizing polarization, correcting coupling, and creating the necessary vertical emittance ratio in the design of the EIC-ESR. These BAGELS knobs will be provided to the control room for operational optimizations. BAGELS will find similar utility in any present or future polarized lepton ring.

References

[1] E. C. Aschenauer. Plans for Early Science. Electron-Ion Collider Machine Advisory Committee Meeting, 2025.

[2] V. N. Baier and V. M. Katkov. Quantum effects in magnetic bremsstrahlung. *Physics Letters A*, 25(7):492–493, 1967.

[3] V. N. Baier, V. M. Katkov, and V. M. Strakhovenko. Kinetics of radiative polarization. *Sov. Phys. JETP*, 31(5):908, 1970.

[4] D. P. Barber et al. High spin polarization at the HERA Electron Storage Ring. *Nucl. Instrum. Meth. A*, 338:166–184, 1994.

[5] D. P. Barber, H. Mais, G. Ripken, and R. Rossmanith. A General Harmonic Spin Matching Formalism for the Suppression of Depolarization Caused by Closed Orbit Distortions in Electron Storage Rings. *DESY-85-044*, 3 1985.

[6] D. P. Barber and G. Ripken. *Handbook of Accelerator Physics and Engineering (3rd Edition)*, chapter 2.6.6 - 2.6.8. World Scientific Publishing Company, 2023.

[7] V. Bargmann, L. Michel, and V. L. Telegdi. Precession of the polarization of particles moving in a homogeneous electromagnetic field. *Phys. Rev. Lett.*, 2:435–436, May 1959.

[8] A. W. Chao. Evaluation of radiative spin polarization in an electron storage ring. *Nucl. Inst. and Meth.*, 180(1):29–36, 1981.

[9] Ya. S. Derbenev and A. M. Kondratenko. Polarization kinematics of particles in storage rings. *Sov. Phys. JETP*, 37:968–973, 1973.

[10] B. Ghojogh, F. Karray, and M. Crowley. Eigenvalue and generalized eigenvalue problems: Tutorial, 2023.

[11] G. H. Hoffstaetter. *High-Energy Polarized Proton Beams: A Modern View*, volume 218. 01 2006.

[12] Vladimir N Litvinenko and A. A. Zholents. Compensating effect of solenoids with quadrupole lenses, 2018.

[13] D. Marx et al. Designing the EIC Electron Storage Ring Lattice for a Wide Energy Range. In *Proc. IPAC'22*, number 13 in International Particle Accelerator Conference, pages 1946–1949. JACoW Publishing, Geneva, Switzerland, 7 2022.

[14] D. Marx et al. Lattice design of the EIC electron storage ring for energies down to 5 GeV. In *Proc. IPAC'23*, number 14 in International Particle Accelerator Conference, pages 104–107. JACoW Publishing, Geneva, Switzerland, 9 2023.

[15] Aaron Meurer, Christopher P. Smith, Mateusz Paprocki, Ondřej Čertík, Sergey B. Kirpichev, Matthew Rocklin, AMiT Kumar, Sergiu Ivanov, Jason K. Moore, Sartaj Singh, Thilina Rathnayake, Sean Vig, Brian E. Granger, Richard P. Muller, Francesco Bonazzi, Harsh Gupta, Shivam Vats, Fredrik Johansson, Fabian Pedregosa, Matthew J. Curry, Andy R. Terrel, Štěpán Roučka, Ashutosh Saboo, Isuru Fernando, Sumith Kulal, Robert Cimrman, and Anthony Scopatz. Sympy: symbolic computing in python. *PeerJ Computer Science*, 3:e103, January 2017.

[16] V. Ptitsyn. *Spin Matching*, pages 183–195. Springer International Publishing, Cham, 2023.

[17] D. Sagan. Bmad: A relativistic charged particle simulation library. *Nuclear Instruments and Methods in Physics Research Section A: Accelerators, Spectrometers, Detectors and Associated Equipment*, 558(1):356–359, 2006. Proceedings of the 8th International Computational Accelerator Physics Conference.

[18] D. Sagan and D. Rubin. Linear analysis of coupled lattices. *Phys. Rev. ST Accel. Beams*, 2:074001, Jul 1999.

[19] M. Sands. The Physics of Electron Storage Rings: An Introduction. *Conf. Proc. C*, 6906161:257–411, 1969.

[20] M. G. Signorelli, Y. Cai, A. E. Connelly, G. H. Hoffstaetter, J. Kewisch, D. Marx, C. Montag, V. Ptitsyn, and S. Tepikian. Polarization preservation methods for the Electron Storage Ring of the EIC. *JACoW*, IPAC2024:MOPC83, 2024.

[21] M. G. Signorelli and G. H. Hoffstaetter. Different forms of first order spin-orbit motion and their utility in spin matching in electron storage rings, 2024.

[22] M. G. Signorelli, G. H. Hoffstaetter, J. Kewisch, and J. A. Crittenden. Spin Matching for the EIC's Electrons. In *Proc. IPAC'22*, number 13 in International Particle Accelerator Conference, pages 2369–2372. JACoW Publishing, Geneva, Switzerland, 7 2022.

[23] M. G. Signorelli, G. H. Hoffstaetter, and V. Ptitsyn. Electron polarization preservation in the EIC. *JACoW*, IPAC2023:MOPA052, 2023.

[24] M. G. Signorelli, G. H. Hoffstaetter, and D. Sagan. Nonlinear Coupling Resonances in the EIC Electron Storage Ring. presented at the 14th Int. Particle Accelerator Conf. (IPAC'23), Venice, Italy, May 2023, paper MOPA051, 5 2023.

[25] A. A. Sokolov and I. M. Ternov. On Polarization and Spin Effects in the Theory of Synchrotron Radiation. *Sov. Phys. Doklady*, 8:1203, June 1964.

[26] L. H. Thomas. I. the kinematics of an electron with an axis. *Phil. Mag.*, 3(13):1–22, 1927.

[27] L. H. Thomas. Recollections of the discovery of the Thomas precessional frequency. *AIP Conference Proceedings*, 95(1):4–12, 1983.

[28] F. Willeke and J. Beebe-Wang. Electron ion collider conceptual design report 2021. 2 2021.

[29] A. Wolski. Alternative approach to general coupled linear optics. *Phys. Rev. ST Accel. Beams*, 9:024001, Feb 2006.